J. Earth Syst. Sci. (2020)129 79
https://doi.org/10.1007/s12040-019-1323-2

Phase petrographic, thermobarometric and petrochemical significance of Cretaceous mafic dykes along Nongchram Fault Zone of Swangkre–Rongmil area of Shillong plateau, NE India: Implications for genetic link to Kerguelen mantle plume

Niva Rani Devi*

Arya Vidyapeeth College, Guwahati, Assam, India.
e-mail: nrdevi@rediffmail.com

MS received 4 July 2018; revised 20 October 2019; accepted 25 October 2019

The present study elucidates the phase petrographic and petrochemical signatures of a group of Cretaceous mafic dykes emplaced in the Precambrian gneissic basement complex in the western part of the Shillong plateau, NE India, in order to trace their petrological, geotectonic, geothermobarometric and oxybarometric status. The whole rock geochemistry discriminates the dykes as basaltic andesites and basaltic trachyandesites genetically related to each other and derived from common parent magma. The enrichment in LREE relative to HREE and HFSE, systematic Nb anomalies, moderate MREE to HREE fractionation suggests variable depths of melting of slightly enriched mantle source in the garnet stability field. As per geochemical modelling, the studied dykes are derived by 3–5% non-modal batch melting of garnet peridotite source at melting depth of ∼65–80 km. The clinopyroxene thermobarometry reveals a temperature span of 1250–800°C and < 2 kb pressure of crystallization for the dykes. The oxygen fugacity (16.82–18.25) indicates extremely reducing conditions at the time of cooling. The very good correlation of petrochemical and phase chemical data with Kerguelen plume derived Rajmahal Group II basalt, Sylhet volcanics and some ODP (ocean drilling project) sites from Kerguelen basalts implicate a genetic link of the studied dykes with Kerguelen mantle plume. Finally, the present study deciphers subalkaline nature of the studied dyke rocks that have been generated by tholeiitic magmas probably in an anorogenic extensional environment. But we need more geochemical data especially good isotope geochronologic data to get a clear picture of the studied dyke.

Keywords. Phase petrography Nongchram fault; Shillong plateau; Kerguelen plateau.

1. Introduction

The chemical composition of mafic dykes and sills occurring in a wide variety of geological and tectonic settings provide clues to their crustal emplacement conditions that may be related to the prevalent tectonic stress regimes (Bondre *et al.* 2006; Duraiswami and Shaikh 2013; Robertson *et al.* 2016). They are considered as ideal geological markers as they serve as conduits for transfer of

Supplementary materials pertaining to this article are available on the Journal of Earth Science Website (http://www.ias.ac.in/Journals/Journal_of_Earth_System_Science).

Published online: 26 February 2020

voluminous magma from the mantle to upper crust and form an important part of the magmatic plumbing system (Delaney *et al.* 1986; Ernst *et al.* 1995). Mafic dykes and dyke swarms are episodic and widespread in almost all the Archean cratons of the Indian shield (Murthy 1987; figure 1). The Shillong plateau plays a vital role in the geological history of the Indian plate. The magmatic history and mafic emplacements of Shillong plateau are important as the plateau forms the northeastern margin of the Indian peninsula and records evidence of the evolving plate boundary. The Shillong plateau is criss-crossed by numerous lineaments in NE–SW, N–S and E–W directions (Chattopadhyay and Hashimi 1984). At least two groups of mafic dykes are established in the Shillong plateau of NE India: older Proterozoic dolerite dykes related to Khasi Greenstone being subjected to low grade metamorphism and a younger Cretaceous group of dykes which are well exposed in West Garo, East Garo and South Khasi Hills districts of Meghalaya in NE–SW, NW–SE and N–S directions (Ray *et al.* 2013; Sarma *et al.* 2014, 2015; Devi 2018).

Although substantial research has already been done in cases of continental flood basalts (CFB) of Deccan Trap, Sylhet Trap and Rajmahal Trap and some parts of Shillong plateau, little information is available on the Cretaceous mafic dykes of Garo Hills, districts of Meghalaya except a few (Rao 2002; Srivastava and Sinha 2004; Rao *et al.* 2009; Devi 2018) in the light of geochemistry and paleomagnetism. The study of phase chemistry and geothermobarometry of Swangkre–Rongmil mafic dykes have not been done in detail. The main

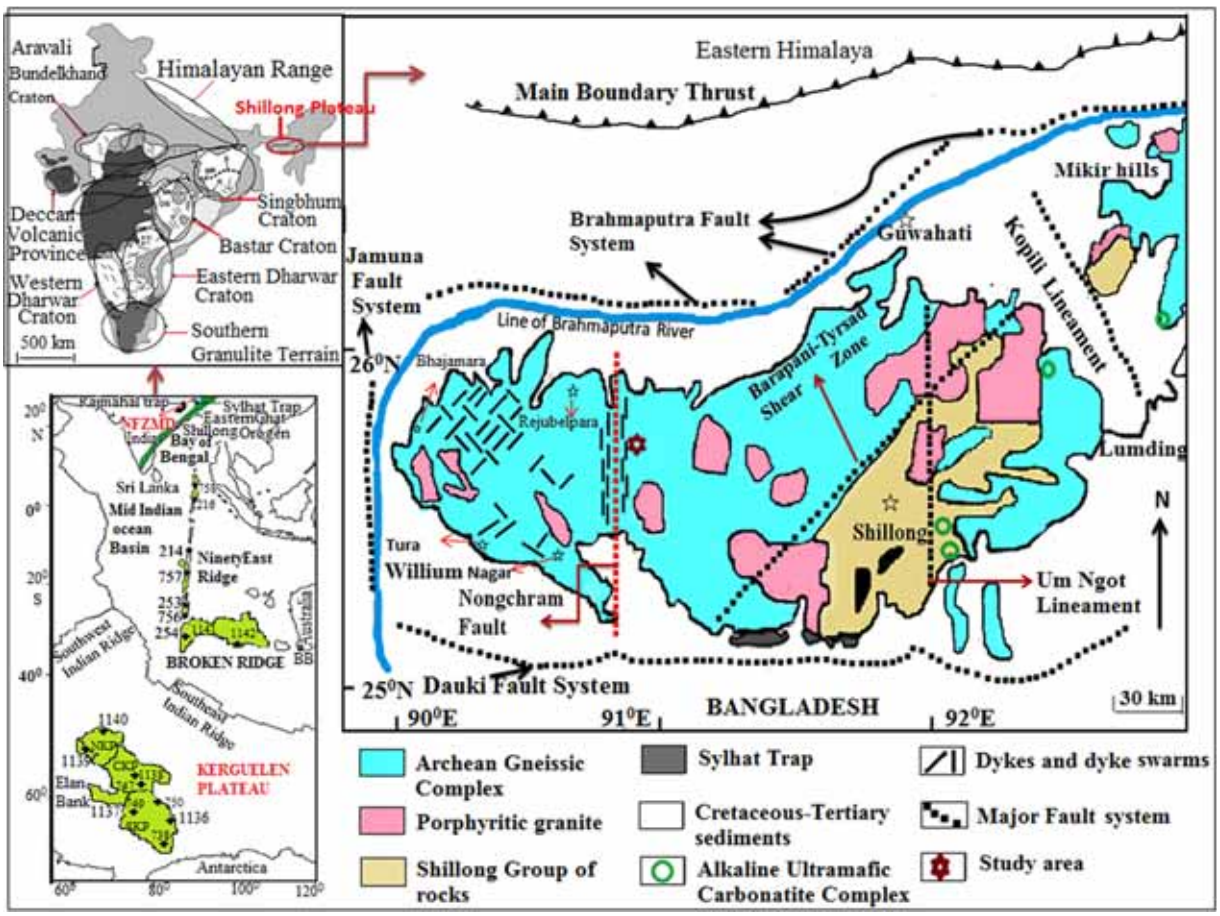

Figure 1. Generalised geological map of Shillong plateau showing dyke and dyke swarms and different faults (from Devi 2018 modified after Srivastava and Sinha 2004; Rao *et al.* 2009) The dyke swarms reported from Indian shield (after French *et al.* 2008; Srivastava *et al.* 2008) is shown as inset (top left). A Map of part of the Indian Ocean and surrounding continents with physiographic features, after Ingle *et al.* (2002b), Frey *et al.* (2000) and (Ghatak and Basu 2011), displaying locations of the Sylhet Trap, Rajmahal Traps and studied dykes (NFZMD) in northeastern India is shown as inset (bottom left). Abbreviations used: BB: Bunbury Basalt drill core sites; NKP: North Kerguelen plateau; CKP: Central Kerguelen plateau; SKP: South Kerguelen plateau; CG: Chilka Granulites (Chakrabarty *et al.* 2011). Black crosses are ODP sites.

impetus of the present work is to generate phase chemical, petrochemical and petrographic information to understand geothermobarometric, oxybarometric and geotectonic status of Swangkre–Rongmil mafic dyke rocks to trace their origin and emplacement history.

2. Regional geological setting

The Shillong plateau (SP), bordered by Brahmaputra lineament to the north, NE–SW trending Naga–Disang thrusted Schuppen Belt (Indo-Myanmar mobile belt, IMMB) to the east, E–W trending Dauki thrust to the south and Dhubri–Yamuna lineament to the west is confined to latitude 25–26°N and longitude 90–93°E and represents a Precambrian cratonic block of North Eastern Indian Region (NEIR), which is believed to be detached from the Indian shield by the Garo Rajmahal tectonic depression (Ermenco *et al.* 1969; Nandy 2001). The uparching of the Meghalaya plateau forming a horst has resulted in the generation of the extensive fault system (Mitra 1998). The uplift is related to collision of the Indian and Tibetan plates during the Cenozoic period (Jhonson and Alam 1991; Bilham and England 2001; Nandy 2001). The E–W trending SP is separated from Mikir hills in the northeast by NW–SE trending Kopili fault system (Evans 1964; Dasgupta and Nandy 1982; Acharyya *et al.* 1986, figure 1). Besides the boundary faults, SP is crisscrossed by numerous lineaments in NE–SW, N–S and E–W directions (Chattopadhyayaa and Hashimi 1984). Some deep faults that are reported from the SP include N–S trending Nongchram fault (Nambiar and Golani 1985; Gupta and Sen 1988; Golani 1991), N–S trending Um Ngot lineaments (Gupta and Sen 1988) and NE–SW trending Barapani–Tyrsad shear zone, Chedrang fault and Raibah fault, Kopili lineaments related to tectonic forces from both the Himalayan collision zone and the Indo-Burma Subduction zone (Kayal 2001; Islam *et al.* 2014). The region is still active due to continued north to northeastward counter clockwise movement of the Indian plate against the Eurasian plate producing intense compressional tectonism (Harijan *et al.* 2003). In spite of significant research carried out on the Shillong plateau (SP) several questions regarding the plateau bounding faults, their origin and major earthquake producing deformation are yet to be satisfactorily answered (Johnson and Alam 1991; Bilham and England 2001; Srinivasan 2005; Rajshekhar and Mishra 2008).

The Basement Gneissic Group (BGG) including quartzofeldspathic gneisses, amphibolites, granulites, calc-silicate rocks, schistose and gneissose rocks of basic to acid composition and Shillong Group of rocks deposited in the intracratonic Shillong basin mainly control the entire lithological setting of Shillong plateau (figure 1, Srivastava and Sinha 2004; Devi and Sarma 2006, 2010; Sarma *et al.* 2014, 2015; Devi 2018). The Sylhet Traps, late Jurassic to Cretaceous sedimentary rocks and Tertiary sedimentary rocks are the other components partly observed towards south, eastern and northeastern part of the plateau.

The dyke swarms in SP are directionally parallel to the major tectonic structures. This suggests their emplacement along fractures, which might have originated due to prevailing extensional tectonics. The mafic dykes, the kernel of present study belong to Swangkre mafic-alkaline-carbonatite dyke swarm and have been emplaced within the Precambrian Basement Gneissic Group (BGG) in the western part of the Shillong plateau (figure 2a). The dykes are exposed extending from north of the Rongmil of East Garo Hills district to the south of the Swangkre of South Khasi Hills district through Nangberram, Dambo–Rongjeng–Nongchram–Nongchram Iding and cover an area of 150 km^2 (Nambiar 2007; figure 2a). Migmatites hornblende and biotite gneisses, porphyritic granitoids and pink granites are the main lithologies of the BGG in the study area. The N–S trending deep seated Nongchram fault (Nambiar and Golani 1985; Nambiar 1987; Gupta and Sen 1988; Golani 1991) is one of the major structural features of the area. The dykes are directionally parallel to this fault and referred hereafter as Nongchram Fault Zone Mafic Dykes (NFZMD). The studied mafic dykes are melanocratic and fine to medium grained and can be classified as basalt and dolerite (figure 2b). Lamprophyre constitutes the dominant member among the alkaline dyke rocks; other petrological variants include tinguaite, ijolite, trachyte and orthoclasite (Srivastava and Sinha 2004; Nambiar 2007). A carbonatite dyke is also reported near Swangkre (Nambiar and Golani 1985). These dykes show very sharp contact with granitoids and no sign of assimilation is noticed.

Gupta and Sen (1988) clearly stated that alkaline and basic magmatism of the Shillong plateau are spatially and temporally associated with the N–S trending structural features developed during

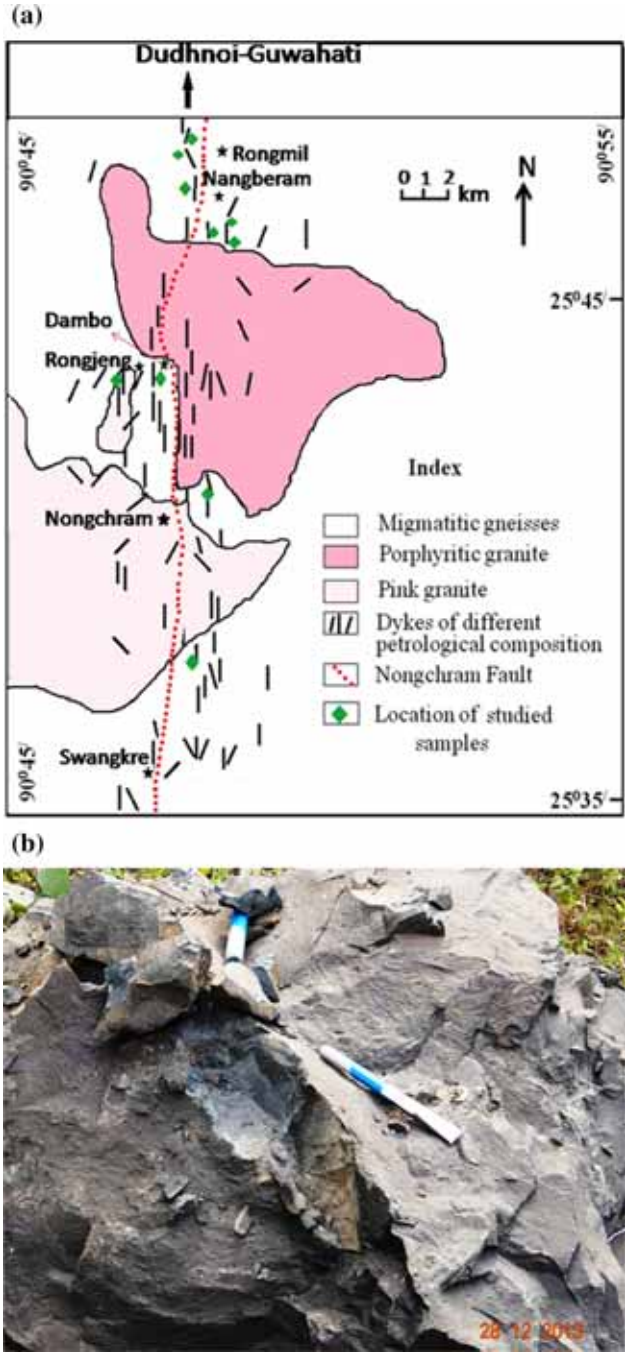

Figure 2. (**a**) Geological map of the study area (from Devi 2018 after Nambiar and Golani 1987; Srivastava and Sinha 2004). (**b**) Field photograph of the studied dyke showing medium grained texture. Location: Nangberram.

the Late Jurassic–Early Cretaceous times. No direct age data is available for the present dykes. Srivastava and Sinha (2004) suggested a relative age for Swangkre–Rongmil mafic dykes based on the available radiometric age data of closely associated lamprophyre dykes (Sarkar *et al.* 1996; Coffin *et al.* 2002) and opined that the mafic dykes might have emplaced around 107–115 Ma.

3. Petrography

Petrographically, the NFZMD rocks are olivine-free fine to medium grained aphyric rocks composed essentially of plagioclase, clinopyroxene and oxide microlites (figure 3a and b). The primary plagioclase and clinopyroxene occur as phenocrysts embedded in a fine-grained groundmass (<1.5 mm) constituted by a variable mixture of glass and cryptocrystalline plagioclase, pyroxene and titaniferous magnetites and other accessories like pigeonite, biotite, k-feldspar, sphene, zircon, calcite, apatite and quartz. Plagioclase phenocrysts generally occurs as lamellar twinned lath shaped grains, but in medium grained variety it may be rectangular to equant and occasionally show compositional zoning. The clinopyroxenes are mostly brownish non-pleochroic augite grains, while pigeonite is found mostly in the groundmass. Clinopyroxene also occur as granules in the intergranular spaces of plagioclase crystals. Opaque phases are marked by magnetite titanomagnetite while ilmenites are confined to the groundmass. Magnetite and Ti-magnetite grains are generally equant, subhedral to euhedral and at places skeletal with occasional exsolution lamellae of ilmenite (figure 3c). Mesostasis consists of devitrified glass containing plagioclase laths, pyroxene granules and platelets of ilmenite. Apatite is present in all dyke rocks as both fine grained, acicular radiating grains and equant grains. Biotite occurs as a subhedral matrix phase. Alteration or secondary phases such as chlorite (after clinopyroxene) and sericite (after plagioclase) are observed in some samples.

Primary igneous texture and structures are well preserved although variable degrees of deuteric and hydrothermal alterations of the primary mineral assemblages are also evident. Texturally the dykes can be grouped into two types such as medium grained doleritic (central part of the dyke) and fine grained basaltic towards the dyke margin types (figure 3a and b). Ophitic and subophitic textures indicating eutectic crystallization between plagioclase and augite are most common in medium grained type (figure 3a). The variation observed in Cpx–Plag ratio may in part reflect flowage differentiation (e.g., Dostal and Durning 1998). Rare occurrences of phenocrystic clots of plagioclase (and often Cpx), possibly with glomeroporphyritic tendencies, are also observed in the medium grained type (figure 3a). Spherulitic texture is another type of texture observed at places (figure 4a). Fine grained variety exhibits

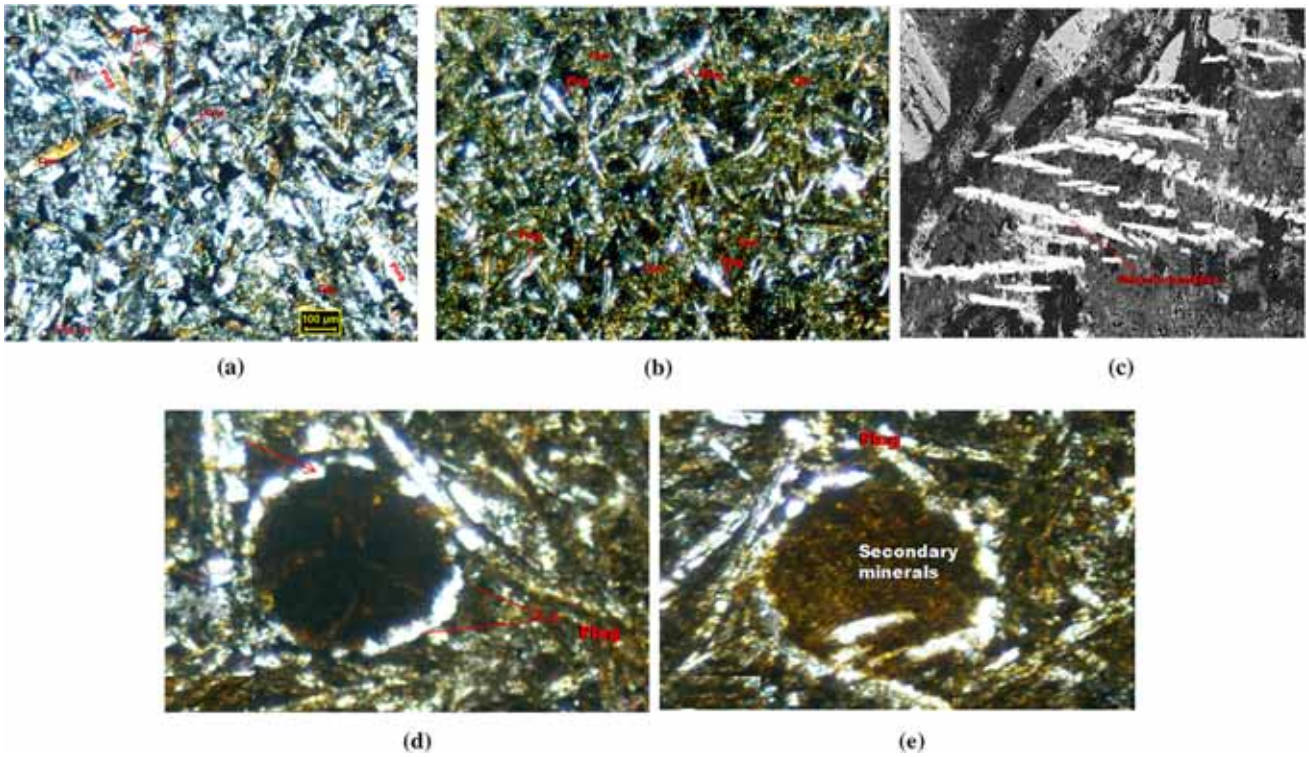

Figure 3. (**a**, **b**) Photomicrographs of medium grained and fine grained variety of the dykes respectively showing phenocrysts of primary plagioclase and clinopyroxene embedded in a fine grained groundmass constituted by a variable mixture of glass and cryptocrystalline plagioclase, pyroxene and titaniferous magnetites and other accessories. Ophitic and subophitic textures exhibited by plagioclase and augite in medium grained type (figure 3b). Fine grained variety displaying intergranular and intersertal textures (figure 3b). (**c**) BSE image of exolution lamelle of ilmenite. (**d–e**) Cavities filled with secondary minerals. Plag laths are arranged concentrically around the cavity.

intergranular and intersertal textures (figure 3b). The marginal portions of these dykes are aphyric and contain devitrified yellowish brown to yellowish green or brown glass. The presence of spherical to ovoid cavities in a few dyke samples is an important feature (figure 3d and e) observed. The cavities are occluded with secondary hydrothermal phases. In addition, plagioclase laths are arranged concentrically around the cavities suggesting a primary origin rather than an alteration induced phenomenon (Kontak *et al.* 2001). These features may represent gas escape feature as the ocelli do in alkaline rocks (Mitchel *et al.* 1991; Le Roex and Lanyon 1998).

4. Analytical procedure

Fresh representative mafic dyke samples are selected for petrochemical study. Whole rock major oxide and trace elements of the selected samples are analysed by X-ray fluorescence (XRF) (Model Simens SRS 3000) at Wadia Institute of Himalayan Geology, Dehradun, India. Fused glass disks are used for the major elements and pressed powder pellets for the trace elements. REE analyses are carried out in the same institute by ICP-MS (Model: Perkin Elmer SCIEX ELAN DRCe). International rock standards JB-1a, the basalt standard produced by GSJ, Japan are also run along with the samples to check precision and accuracy. Sample dissolution for ICP-MS analyses are carried out following the procedure described by Khanna *et al.* (2009). The overall accuracy for major and minor oxide is better than 5% and the precision is better than 2% (Saini *et al.* 2007; Khanna *et al.* 2009).The accuracy for REE is better than 12% and precision is better than 5% (Saini *et al.* 2007, 2013; Khanna *et al.* 2009).

The major element constituents of the minerals are determined by Electron Microprobe Analyzer (EPMA) for identification of mineral species at EPMA Laboratory, Central Headquarters, GSI, Kolkata. The samples are analysed with a CAMECA SX100 instrument at accelerating voltage of 15 kV, current of 12 nA and beam size of 1 μ. Data acquisition and data reduction are done by an online computer. Both synthetic and homogenous

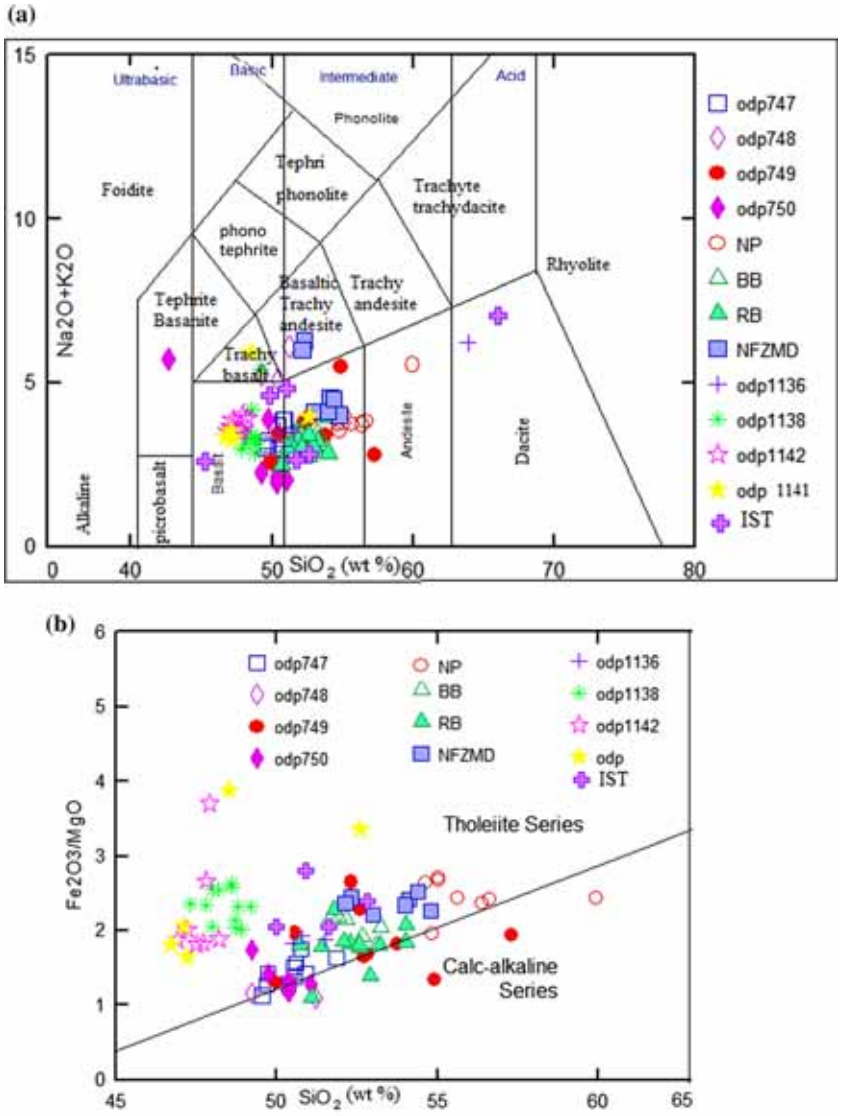

Figure 4. (**a**) Total alkali *vs.* silica plot (after Le Bas *et al.* 1986) for NFZMD, showing basaltic andesitic and basaltic trachyandesitic field; (**b**) SiO_2–FeOt/MgO plot (Myashiro 1974), showing tholeiitic character for the studied dykes. *Data sources*: Frey *et al.* 1996, 2002; Neal *et al.* 2002; Storey *et al.* 1992. Data for Sylhat trap tholeiites (IST) are after Islam *et al.* (2014).

standards are used. The accuracy of EPMA data and oxide total was ±1.5. A total of 75 grains from three samples, including the phenocryst and groundmass are probed from the core to rim for Plag and Cpx and single points at core for Fe–Ti oxides and groundmass glasses.

5. Analytical results

5.1 *Whole rock geochemistry: Major oxide, trace element and REE signatures*

The whole rock geochemistry data are adopted from Devi (2018) for reference. The CIPW normative composition represents the presence of 5.92–15.81wt.% quartz which suggests silica saturated quartz tholeiitic characters of NFZMD (table 1). In the total alkali ($Na_2O + K_2O$) *vs.* silica (SiO_2) diagrams (Le Bas *et al.* 1986) the samples plot in the field of basaltic andesite and basaltic trachyandesite field (figure 4a). The SiO_2 (52.32–54.79 wt.%), moderate MgO (4.68–5.32 wt.%) and CaO (5.02–7.44) wt.% as well as Al_2O_3 content ranging from 12.04 to 13.16 wt.% indicates tholeiitic character of the mafic dykes (table 1). The rocks are typically enriched in Fe with 9.83–10.7 wt.% FeO and plot in the high Fe tholeiitic basalt (Jensen 1976, figure not shown). Tholeiitic character is well depicted in the SiO_2 *vs.* (FeO + MgO) plot of Myashiro (1974) (figure 4b)

Table 1. *Whole rock major oxide (wt.%), trace and REE (PPM) data for mafic dyke rocks of Swangkre–Rongmil area.*

Sample	Na_2O %	MgO %	Al_2O_3 %	SiO_2 %	P_2O_5 %	KO %	CaO %	TiO_2 %	MnO %	$Fe_2O_{3(T)}$ %	Sum %	LOI %	Ba PPM	Cr PPM	V PPM
NB1	3.10	4.95	12.26	54.13	0.28	1.45	7.11	2.00	0.15	12.00	97.43	2.92	489	61	205
NB2	3.97	5.10	12.40	52.32	0.35	2.31	5.02	2.23	0.16	12.47	96.33	3.11	846	34	227
NB3	2.47	5.25	12.50	53.00	0.28	1.65	7.44	1.94	0.14	11.61	96.28	3.25	434	85	202
NB4	2.57	5.12	12.04	54.79	0.28	1.45	7.07	1.99	0.16	11.57	97.04	3.62	429	64	209
NB5	2.70	4.97	13.09	54.01	0.29	1.42	7.10	1.98	0.16	11.65	97.37	3.13	472	59	204
NB6	3.78	5.32	13.05	52.14	0.35	2.23	5.20	2.15	0.16	12.60	96.98	3.43	812	40	223
RM	3.15	4.68	13.16	54.38	0.32	1.37	7.09	2.01	0.15	11.83	98.14	2.25	522	65	203

Sample	Sc PPM	Co PPM	Ni PPM	Cu PPM	Zn PPM	Ga PPM	Pb PPM	Th PPM	Rb PPM	U PPM	Sr PPM	Y PPM	Zr PPM	Nb PPM
NB1	27	34	19	15	135	24.7	5.8	2.5	28	<1.00	311	38	185	12.3
NB2	23	33	10	16	141	21.1	4.4	0.9	89	<1.00	239	45	204	13.2
NB3	23	34	17	17	133	22.7	6.2	3.1	33	<1.00	321	38	182	11.1
NB4	24	30	16	16	138	23.8	5.3	2.7	25	<1.00	333	37	187	11.6
NB5	26	43	18	16	136	23.3	5.4	2.1	25	<1.00	339	38	184	11.5
NB6	22	43	13	17	142	22.1	5.8	2.3	86	0.98	231	46	202	12.3
RM	25	40	19	16	133	24.1	6.5	0.7	25	1.02	352	38	183	11.8

Sample	La PPM	Ce PPM	Pr PPM	Nd PPM	Sm PPM	Eu PPM	Gd PPM	Tb PPM	Dy PPM	Ho PPM	Er PPM	Tm PPM	Yb PPM	Lu PPM
NB1	22.4	49.6	6.7	28.4	7.13	2.32	8.07	1.26	7.21	1.52	3.89	0.58	3.71	0.54
NB2	23.1	51.4	7	30.3	7.32	2.38	8.36	1.31	7.57	1.56	4.06	0.61	3.81	0.59
NB3	21.5	47.7	6.4	27.6	6.81	2.25	7.89	1.24	7.13	1.47	3.81	0.57	3.58	0.54
NB4	21	46.5	6.3	27.5	6.78	2.19	7.77	1.21	7.02	1.42	3.72	0.55	3.53	0.54
NB5	20.9	46.9	6.3	27.1	6.7	2.19	7.66	1.21	6.98	1.43	3.74	0.55	3.48	0.54
NB6	23	51.5	7	29.7	7.31	2.4	8.26	1.3	7.59	1.54	4.03	0.6	3.79	0.58
DRNG	91.9	194.4	23.1	81.6	12.4	3.17	10.7	1.28	6.25	1.26	3.31	0.47	3.18	0.46
NID	88.2	170.5	19.5	70.5	11.1	3.28	10.7	1.34	6.49	1.2	3.05	0.43	2.82	0.41
NOCHA	38.8	86.1	11.1	45.1	10.2	2.83	10.8	1.63	8.98	1.85	4.67	0.67	4.32	0.61
RM	22.4	49.3	6.6	27.8	7.08	2.28	7.97	1.26	7.2	1.53	3.9	0.57	3.71	0.54

Sample	NB1	NB2	NB3	NB4	NB5	NB6	NOCH A	RM
Sum_REE	143.33	149.37	138.49	136.03	135.68	148.6	433.48	142.14
$(La/Sm)_N$	1.93	1.94	1.94	1.91	1.92	1.94	4.56	1.95
(La/Yb)N	4.03	4.04	4	3.97	4	4.05	19.27	4.03
$(Sm/Yb)_N$	2.08	2.08	2.06	2.06	2.08	2.8	4.22	2.07
$(Gd/Yb)_N$	1.73	1.75	1.76	1.75	1.75	1.73	2.68	1.73
Eu/Eu*	0.94	0.94	0.94	0.93	0.94	0.95	0.85	0.93

BDL: below detection limit, total iron as $Fe_2O_{3(T)}$, LOI: loss of ignition.

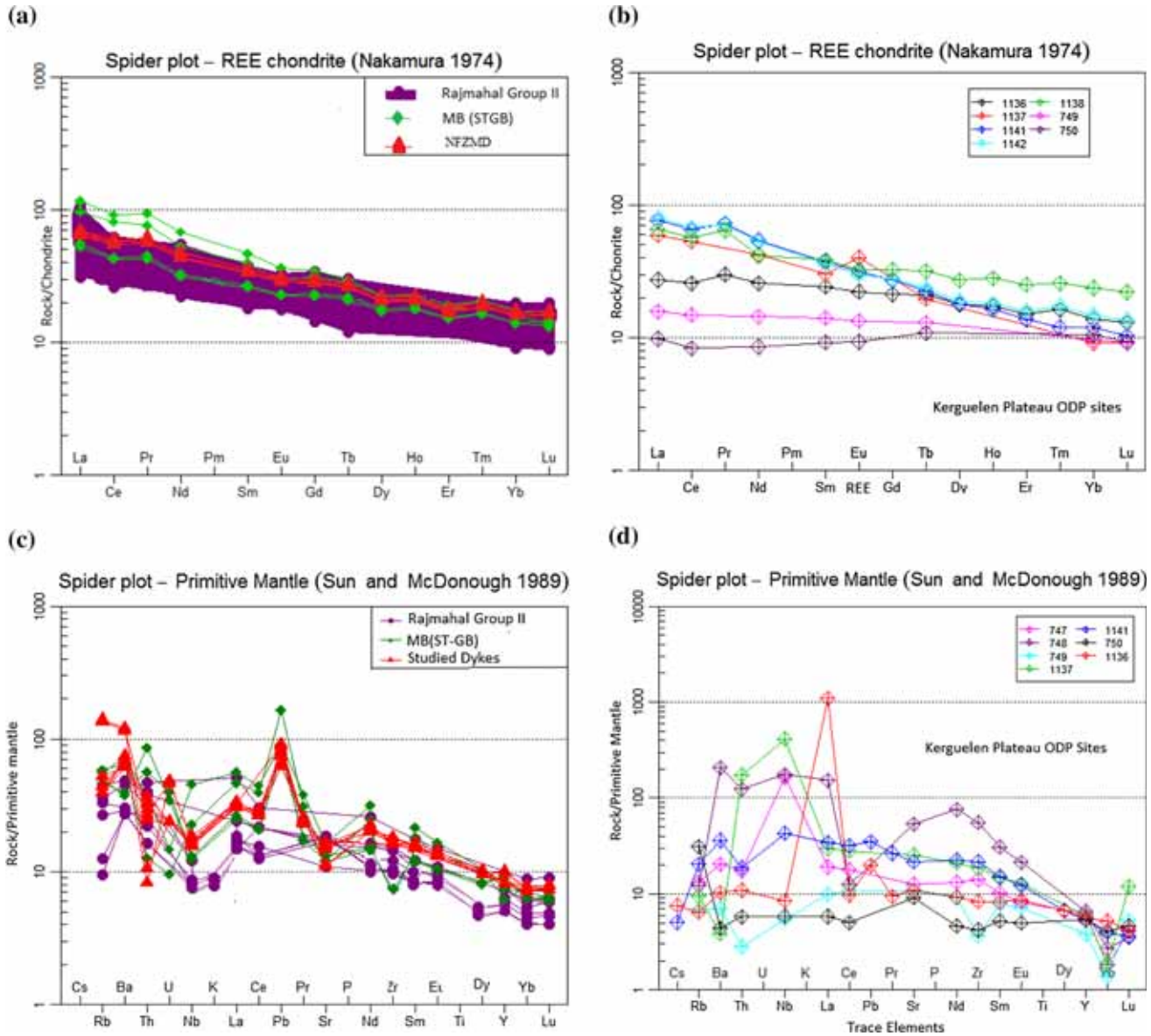

Figure 5. **(a)** Chondrite normalized (Nakamura 1974) REE pattern for NFZMD, Rajmahal Group II basalts, Sylhat trap (MB – data from Ghatak and Basu 2011). **(b)** Chondrite normalized (Nakamura 1974) REE pattern for Kerguelen plateau ODP sites. *Data sources*: 1136, 1138, 1141, and 1142 from Neal *et al.* (2002), 1137 from Ingle *et al.* (2002b), 747, 749 and 750 from Storey *et al.* (2003). **(c)** Primitive mantle normalized (Sun and McDonough 1989) multielement pattern for NFZMD. **(d)** Primitive mantle normalized (Sun and McDonough 1989) multielement pattern for Kerguelen plateau ODP sites.

and AFM diagram of Irvine and Baragar (1971) (figure not shown).

Chondrite normalized REE pattern (Nakamura 1974) of the studied dykes exhibit inclined LREE and relatively flat HREE pattern (figure 5a). Eu anomaly is negligible. It is close to 1. Similar REE pattern is observed for some Kerguelen plateau ODP sites (figure 5b). Primitive mantle normalized (Sun and Mc Donough 1989) multielement pattern indicates consistent trace element characters and suggest an overall geochemical similarities among the samples (figure 5c). Samples show positive Ba and Pb anomalies. Negative anomalies such as Sr, P, Nb, Th, and Yb anomalies are also observed in multielement spidergram. Similar correlation is seen for some Kerguelen plateau ODP sites (figure 5d). The samples are characterized by depletion in compatible elements (Ni, Cr) and relative enrichment in incompatible elements like LILE and LREE (table 1). The concentration of HFSE (high field strength elements) such as Zr (182–204), Nb (11.1–13.2 ppm), Sc (23–27), Y (37–46), Th (0.7–3.1) and U ($\sim$1 ppm) are moderate.

Table 2. *EPMA data of representative Pyroxene composition (wt.%) from different sectors of mafic dykes of Swangkre–Rongmil area.*

Sample	SiO_2	Al_2O_3	MgO	Na_2O	P_2O_5	K_2O	CaO	TiO_2	Cr_2O_3	MnO	FeO	NiO
P-C	47.29	2.35	12.03	0.3	0.2	0.03	15.83	1.69	0	0.39	18.9	0.6
P-C	47.91	2.19	13.34	0.24	0.22	0	15.16	2.59	0	0.35	18.18	0.04
P-C	48.31	2.5	12.18	0.23	0.16	0	16.01	1.84	0	0.36	18.61	0
P-C	48.55	1.72	13.04	0.23	0.23	0.03	14.56	1.35	0.09	0.46	19.76	0.01
P-C	47.77	1.87	12.64	0.24	0.16	0	14.7	1.34	0.09	0.4	19.28	0.04
P-C	48.23	1.67	12.33	0.24	0.24	0.05	14.63	1.38	0.15	0.59	19.59	0.04
P-C	50.77	1.69	15.02	0.26	0.26	0.14	16.39	1.02	0	0.29	15.06	0
P-C	49.99	1.43	13.39	0.3	0.27	0.02	20.08	0.78	0.11	0.49	12.51	0
P-R	46.89	2.41	10.86	0.31	0.21	0.05	15.64	2.18	0	0.4	20.8	0
P-R	49.36	1.75	15.12	0.23	0.23	0	16.74	1.03	0	0.3	14.44	0.06
GM-C	49.18	3.1	15.86	0.21	0.23	0	14.62	1.3	0.09	0.33	14.62	0
GM-C	49.58	2.13	15.75	0.22	0.12	0	12.64	1.26	0.02	0.47	17.92	0
GM-C	42.64	5.63	13.29	0.11	0.03	0.01	4.49	0.38	0.62	0.39	21.21	0
GM-C	48.98	1.9	14.01	0.24	0.23	0.01	15.77	0.99	0.14	0.4	15.22	0.02
GM-R	49.69	2.42	17.44	0.19	0.16	0.04	12.52	1.03	0	0.2	15.89	0
GM-R	50.21	1.96	14.65	0.27	0.25	0.04	18.02	1.07	0	0.26	12.92	0.03
Avg	48.46	2.30	13.81	0.24	0.2	0.03	14.86	1.33	0.08	0.38	17.18	0.05

Sample	Si	Ti	Al	Fe^{3+}	Fe^{2+}	Mn	Mg	Ca	Na	Wo	En	Fs	$Fe^{\#}$	$Mg^{\#}$	Q	J	Q + J
P-C	1.84	0.05	0.11	0.14	0.47		0.7	0.66	0.02	36.07	38.17	25.78	0.47	0.53	0.04	1.83	1.87
P-C	1.83	0.05	0.99	0.1	0.48	0.1	0.76	0.62	0.02	33.4	40.89	25.71	0.43	0.57	0.04	1.86	0.54
P-C	1.86	0.05	0.11	0.09	0.51	0.01	0.7	0.66	0.02	35.37	37.44	27.19	0.46	0.54	0.04	1.87	1.91
P-C	1.87	0.04	0.08	0.13	0.51	0.02	0.78	0.6	0.02	32.36	40.32	27.31	0.45	0.55	0.04	1.89	1.93
P-C	1.86	0.04	0.09	0.13	0.5	0.01	0.74	0.61	0.02	33.15	39.66	27.18	0.46	0.54	0.04	1.85	1.89
P-C	1.88	0.04	0.08	0.11	0.53	0.02	0.72	0.61	0.02	32.86	38.53	28.62	0.47	0.53	0.04	1.86	1.9
P-C	1.9	0.03	0.08	0.09	0.39	0.04	0.84	0.66	0.02	34.92	44.53	20.55	0.36	0.64	0.04	1.89	1.93
P-C	1.9	0.02	0.06	0.11	0.28	0.02	0.76	0.82	0.02	43.96	40.78	15.26	0.34	0.66	0.04	1.86	1.9
P-R	1.83	0.06	0.11	0.14	0.54	0.01	0.63	0.65	0.02	35.76	34.55	29.69	0.52	0.48	0.04	1.82	1.86
P-R	1.87	0.03	0.08	0.14	0.32	0.01	0.86	0.68	0.02	36.61	46.01	17.38	0.35	0.65	0.04	1.86	1.9
GM-C	1.85	0.04	0.14	0.09	0.37	0.01	0.89	0.59	0.02	31.93	48.19	19.88	0.34	0.66	0.04	1.85	1.89
GM-C	1.87	0.04	0.12	0.1	0.46	0.02	0.89	0.51	0.02	27.48	47.65	24.87	0.39	0.61	0.04	1.86	1.9
GM-C	1.84	0.01	0.29	0.01	0.75	0.01	0.85	0.21	0.01	11.42	47.01	41.57	0.47	0.53	0.02	1.81	1.83
GM-C	1.9	0.03	0.09	0.08	0.41	0.01	0.81	0.65	0.02	34.89	43.13	21.98	0.38	0.62	0.04	1.87	1.91
GM-R	1.86	0.03	0.11	0.12	0.38	0.01	0.97	0.5	0.01	27.12	52.57	20.31	0.34	0.65	0.02	1.85	1.87
GM-R	1.9	0.03	0.09	0.09	0.32	0.01	0.82	0.73	0.02	38.89	43.99	17.12	0.33	0.67	0.04	1.87	1.91
Avg	1.87	0.04	0.16	0.10	0.45	0.02	0.80	0.61	0.02	32.89	42.71	24.4	0.41	0.59	0.08	1.87	1.81

All Fe as FeO, $Fe^{\#} = Fe^t/Fe^t + Mg$; $Mg^{\#} = Mg/Mg + Fe^t$; Wo = Wollastonite; En = Enstatite; Fs = Ferrosilite; Q = 2 Na; J = Ca + Mg + Fe^{2+}; PC: PhenocrystCore; PR: Phenocryst rim; GMC: Groundmass core; GMR: Groundmass rim.

Table 3. *EPMA results of average value of major oxides (wt.%) of Plag of dyke rocks from different sectors of study area.*

Phenocryst	Core	Rim	Core	Rim	Core	Rim	Core	Rim
SiO_2	53.97	52.54	54.56	57.26	55.56	57.43	57.88	54.88
Al_2O_3	27.1	27.24	27.15	25.89	27.31	26.07	25.31	26.91
MgO	0.13	0.44	0.18	0.11	0.19	0.07	0.04	0.14
Na_2O	5.18	4.69	5.09	6.12	5.23	6.09	6.29	5.37
P_2O_5	0.13	0.15	0.16	0.1	0.16	0.06	0.18	0.15
K_2O	0.38	0.31	0.35	0.58	0.35	0.55	0.66	0.46
CaO	10.6	11.06	10.78	8.84	10.57	8.99	8.34	10.63
TiO_2	0.08	0.09	0.12	0.09	0.14	0.04	0.08	0.16
Cr_2O_3	0.07	0.04	0.04	0	0	0	0	0
MnO	0.02	0.03	0.07	0.01	0.1	0	0	0.03
FeO	0.76	0.76	0.67	0.85	0.68	0.77	0.83	0.76
NiO	0.01	0	0	0	0	0	0	0.01
Total	98.43	97.35	99.17	99.85	100.3	100.08	99.59	99.51
Cations on 8 oxygen basis and Ab, An and Or are in Mole %								
Si	2.5	2.47	2.51	2.6	2.52	2.62	2.63	2.52
Al	0.73	1.51	1.47	1.39	1.46	1.35	1.36	1.46
Ca		0.79	0.77	0.63	0.76	0.64	0.6	0.76
Na		0.43	0.45	0.54	0.46	0.54	0.55	0.48
K		0.02	0.02	0.03	0.02	0.03	0.04	0.03
An	68.3	71.4	69.1	60	68.1	60.6	57.8	67.4
Ab	30.2	27.4	29.5	37.6	30.5	37.2	39.5	30.8
Or	1.5	1.2	1.3	2.3	1.3	2.2	2.7	1.7

Total Fe expressed as FeO; Ab = 100 × Na/(Na + K+Ca); Or = 100 × K/(Na + K+Ca); An = 100 × Ca/(Na + K+Ca).

5.2 *Phase chemistry of the dykes*

The study of the mineral and glass compositions plays a vital role to decipher different magma types as well as their eruption and crystallization histories. The main phases clinopyroxene and plagioclase along with associated opaque oxides and glasses of NFZMD were considered in the present study. The analyses of clinopyroxene (Cpx), plagioclase (Plag), magnetite, titaniferous magnetite and ilmenite are furnished in the tables (tables 2–5).

5.2.1 *Pyroxenes (Cpx)*

Clinopyroxene occurs predominantly as subhedral phenocrysts, microcrysts and granules in the intergranular spaces of plagioclase crystals. Cations and structural formula of Cpx are calculated on the basis of six-oxygen and four cations following the procedure of Lindsley (1983). While plotted data in the quadrilateral classification diagram Di–Hd–En–Fs (Morimmoto 1988) all analyses in cores and rims of both phenocrysts and groundmass fall in the Augite field with an average end member composition of $Wo_{34}\,En_{42}Fs_{23}$ and rare occurrence of pigeonite with $En_{47.01}Wo_{11.42}Fs_{41.57}$ (figure 6a). The entire analyzed Cpx plot within the Ca–Mg–Fe pyroxene (quad area) field in the Q–J pyroxene classificatory diagram (figure 6b). There is a slight decrease of MgO and CaO contents at the core relative to the rim, and slight increase of FeO at rim relative to the core in both phenocryst and groundmass observed in the variation diagram of SiO_2 *vs.* MgO, FeO(*t*) and CaO (figure S1a–c, table 2). But normal or reverse compositional zoning of Cpx grains is not clear. Some overlap between groundmass and phenocryst compositions observed in the figure indicates the simultaneous crystallization of both phenocryst and groundmass. Sometimes clinopyroxenes show high Mg core against other low Mg cores and rims containing higher Mg or vice versa indicates the oscillatory conditions of crystallization from the source magma.

5.2.2 *Plagioclase (Plag)*

Plag phenocrysts are lath shaped, lamellarly twined and occasionally show compositional zoning. The content of An in the phenocrysts of plagioclase varies

Table 4. *EPMA data of representative phenocrysts (cores) of magnetite and ilmenite.*

Fe-oxides	Magnetite	Ilmenite	Magnetite	Ti-magnetite	Magnetite
SiO_2	0.9	0.14	4.54	6.8	7.4
Al_2O_3	0.05	0.02	0.62	0.86	1.02
MgO	0.14	0	0	0.07	0.16
Na_2O	0.08	0	0.05	0.06	0.08
P_2O_5	0	0	0	0.12	0.01
K_2O	0.05	0.12	0.03	0.07	0.04
CaO	0.36	0.3	3.88	4.82	4.81
TiO_2	17.29	50.38	8.3	34.16	6.7
Cr_2O_3	0.06	0	0	0	0
MnO	0.41	5	0.46	1.48	0.28
FeO	72.05	44.21	74.72	55.65	73.21
NiO	0.05	0.08	0	0.02	0
Total	91.45	100.26	92.6	104.09	93.7
No. of ions of magnetite and ilmenite calculated on 4 and 3 oxygen basis, respectively					
Si	0.004	0.004	0.173	0.233	0.276
Ti	0.524	0.955	0.238	0.88	0.188
Al	0.002	0.001	0.279	0.035	0.045
Fe^{3+}	0.947	0.081	1.146	0.264	1.027
Fe^{2+}	1.448	0.851	1.237	1.858	1.253
Mn	0.014	0.107	0.015	0.043	0.009
Mg	0.008	0	0	0.034	0.009
Ca	0.016	0.001	0.159	0.177	0.192
Na	0.006	0	0.004	0.004	0.006
K	0.003	0.004	0.002	0.003	0.005
Recalculated analysis of ulvospinel and ilmenite basis					
Fe_2O_3	30	4.6	40	–10.2	36.7
FeO	44.2	40	38.8	64.2	40.2

The calculation of molecular percentages of ulvospinel and ilmenite were done by ILMAT, a magnetite–ilmenite geothermometry Program (version 1.20) formulated by Lepage (2003) based on the recalculation schemes of Carmichael (1967), Anderson (1968), Lindsley and Spencer (1982) and Stormer (1983).

Table 5. *EPMA results of representative glass composition (wt.%) of the mafic dykes.*

Oxides	SiO_2	Al_2O_3	MgO	Na_2O	P_2O_5	K_2O	CaO	TiO_2	Cr_2O_3	MnO	FeO	NiO	Total
Glass	67.63	12.44	1.29	2.9	2.03	2.8	4.97	0.39	0.15	0.01	3.93	0	98.53
Glass	70.58	14.56	0.05	4.62	0.17	2.38	2.46	0.58	0	0.02	0.96	0	96.37
Glass	67.94	8.68	0.65	1.61	1.03	4.48	2.6	2.73	0.05	0.31	7.94	0	98.02
Glass	75.38	11.62	0.04	2.59	0.15	6.83	0.55	0.1	0	0.01	0.51	0.04	97.83
Glass	73.98	12.49	0	2.47	0.16	7.22	0.5	0.36	0.09	0.07	0.88	0	98.23
Glass	71.93	9.82	0.09	1.64	0	5.42	0.29	0.12	0.9	0	1.69	0	91.89
Glass	78.17	9.16	0	2.1	0	5.45	0.96	0.87	0.01	0	0.38	0	97.1
Glass	61.45	23.41	0.03	8.6	0	2.47	0.58	0.01	0.1	0	0.43	0	97.08
Average	70.8825	12.7725	0.26875	3.31625	0.4425	4.63125	1.61375	0.645	0.1625	0.0525	2.09	0.005	96.88125

from 61.6 to 71.4% in core and 63.2 to 85.3% in rim, while it is in groundmass, varying from 51.5 to 57.8% in core and 59.6 to 68.7% in rim (table 3). In the ternary classification diagram Ab–An–Or the overall measured range of Plag composition plots very close to the An–Ab join due to low amounts of orthoclase component (< 2.7%, figure 7). The narrow difference in An content between the core (low) and rim (high) of both phenocryst and groundmass grains indicate weak reverse chemical zoning. Some overlap between groundmass and phenocryst compositions observed in the figure indicates the simultaneous crystallization of both phenocryst and groundmass. Individuals relatively rich in An component (up to 71.4%) may

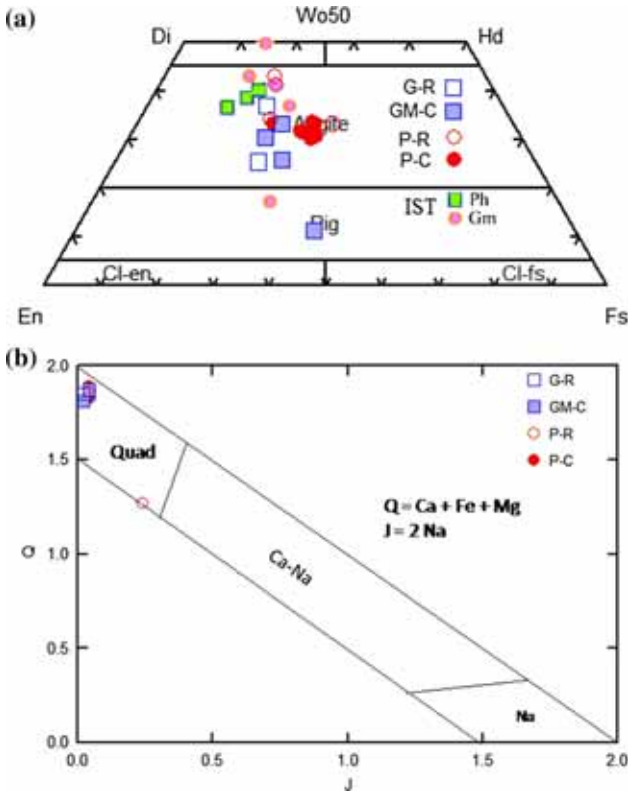

Figure 6. (**a**) Classification diagram of Di–Hd–En–Fs for pyroxenes. PC, PR, GC and GR denote phenocryst core, phenocryst rim, groundmass core and groundmass rim. Plot of investigated pyroxene compositions of NFZMD samples in wollastonite (Wo)–Enstatite (En)–Ferrosilite (Fs) diagram (Morimmoto 1988). Cpx data for Sylhat trap tholeiites (IST) after Islam *et al.* (2014) are shown for comparison. (**b**) Plot of pyroxene compositions of NFZMD samples in Q–J diagram (Morimmoto 1988).

be the petrographic evidence to confirm that the Plag was the liquidus phase. It is evident from figure that SiO_2 shows weak negative correlation with CaO and Al_2O_3 and positive correlation with Na_2O (figure S2a–c). The overall An content of 67.4–71.4% (in phenocryst core) and 57.8–60.6% (in phenocryst rim) reflects that the parent magma from which the dyke rocks are derived is of tholeiitic composition.

5.2.3 *Magnetite and ilmenite*

The opaque minerals in studied dykes are mainly ilmenite, magnetite and rarely titaniferous magnetite. The samples have average weight percentages for FeO (total) around 73.32% in magnetite and 44.21% in ilmenite as well as TiO_2 10.76% in magnetite and 50.38% in ilmenite (table 4). The Fe^{2+}, Fe^{3+} and Ti components when plotted in a triangular diagram indicates both magnetite and ilmenite field (figure 8). The grains have distinct grain boundaries and no apparent chemical alteration and visually distinct zoning are marked. The compositions of the grains were fairly consistent in three samples regardless of grain size (table 4).

5.2.4 *Glass*

The observed composition of glass that constituted the interstitial parts of the groundmass of the studied rocks ranges from dacite to rhyolite, according to their classification using the T.A.S. diagram (figure not shown; table 5).

6. Discussion

6.1 *Petrogenesis*

The wide range of major and trace element composition represented by the mid- to high-Ti basalts of present study are used to study various igneous processes such as partial melting, fractional crystallization and possibly crustal contamination.

6.1.1 *Status of mantle melting*

Trends of compatible and incompatible trace element may be used successfully to evaluate melting or differentiation processes for generation of different mafic magmas in the upper mantle (Rajamani *et al.* 1985; Condie *et al.* 1987). Allegre and Minster (1978) showed that the ratio of the concentration of a highly incompatible element can identify partial melting trends. A very good linear correlation of NFZMD in Th/Nb *vs.* Th diagram shows that they were probably generated by partial melting of distinct mantle source (figure 9a). Rajamani *et al.* (1985) suggested that a rock suite generated from different degrees of melting of the same source should have similar trend to melting curves. The model based on binary plot of Zr *vs.* Ni (Rajamani *et al.* 1985), is used for the present mafic dykes (figure 9b), which suggests a single magma source responsible for NFZMD. The magma generated by ∼5– <10% melting of a mantle followed by more than 50% fractional crystallization led to the formation of these mafic dykes. The presence of garnet in the partial melting residue can lead to strong LREE enrichment of the melt. The REE signatures of NFZMD marked by $(La/Sm)_N$ 3.09–3.80, $(La/Yb)_N$ 3.97–4.05, $(Sm/Yb)_N$ 2.04–2.09 and $(Gd/Yb)_N$ 1.71–2.39 (table 1) with chondrite-normalized REE patterns reflect LREE

Table 6. *Equilibration temperature (°C), pressure (kbar) and oxygen fugacity of mafic dykes.*

Methods adopted	T (°C) range	Pressure (kbar)	Remarks	Basis
Pyroxene geothermobarometers				
Lindsley (1983)	800–1250	NA	Ideal igneous temperature	Graphical method
Soesso (1997)	1050–1150	<2		Graphical method
Putrika (1996): eqn T_1 and eqn T_2	1003–1030	***		Based on Cpx-liquid composition only
Putrika *et al.* (2003)	1050	***		
Putrika (2008): eqn 32d (T) and 32a (P)	903.2	1.8		Based on Cpx composition only
Putrika (2008): eqn 32d (T) and 32c (P)	1045	1.2		
Putrika (2008): eqn 33 (T)	975.4	***		
Putrika (2008): eqn 34 (T)	1116.3	***		
Nimis and Taylor (2000)	995–997.5	***		
Heltz (1973)		<5		Based on Al^{vi}/Al^{iv} plot of Cpx
Aoki and Shiba (1973)		Low pressure field		Based on Al^{iv}/Al^{vi} plot of Cpx

Methods adopted	Methods of recalculations of Mol%	Mol% USP	Mole% Ilm	T (°C)	($\log_{10} fO_2$)
Magnetite–ilmenite geothermometer					
Powel and Powel (1977)	Carmichael (1967)	52.75	95.82	798	
	Anderson (1968)	52.32	95.32	813	
	Lindsley and Spencer (1982)	53.11	95.32	817	
	Stormer (1983)	52.17	95.72	798	
Spencer and Lindsley (1981)	Carmichael (1967)	52.75	95.82	695	– 18.25
	Anderson (1968)	52.32	95.32	723	– 17.28
	Lindsley and Spencer (1982)	53.11	95.32	727	– 17.18
	Stormer (1983)	52.17	95.72	698	– 18.1
Anderson and Lindsley (1985)	Carmichael (1967)	52.75	95.82	721	
	Anderson (1968)	52.32	95.32	745	– 16.89
	Lindsley and Spencer (1982)	53.11	95.32	749	– 16.82
	Stormer (1983)	52.17	95.72	724	– 17.59

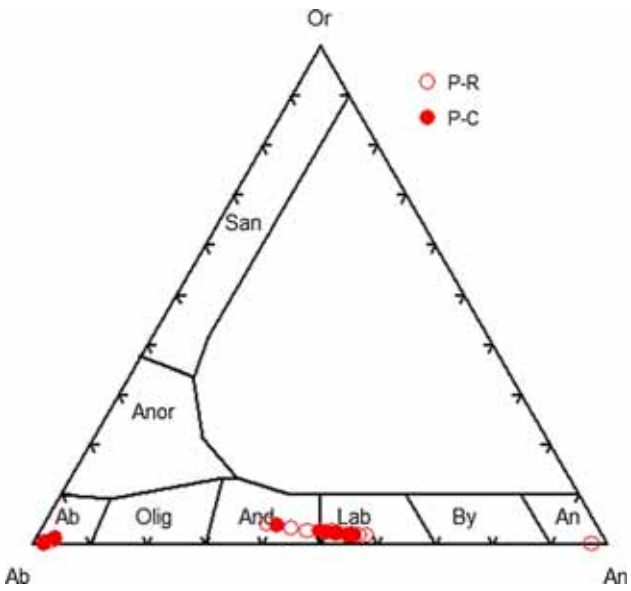

Figure 7. Ternary classification diagrams of Ab–An–Or for feldspars. PC, PR, GC and GR denote phenocryst core, phenocryst rim, groundmass core and groundmass rim.

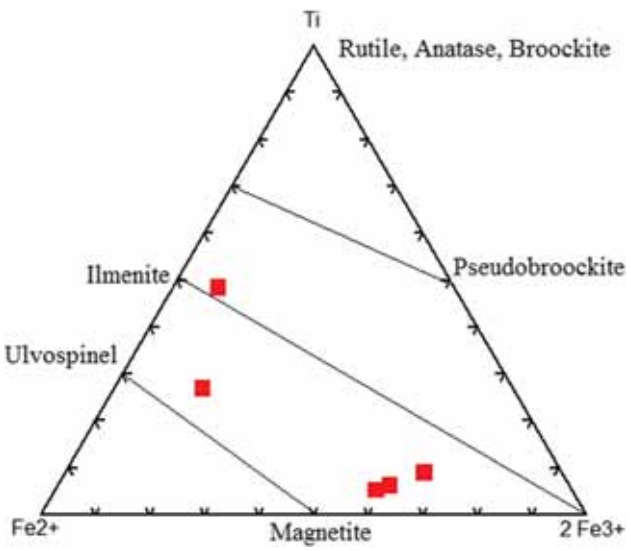

Figure 8. Classification of magnetite and ilmenite based on variations of atomic proportions of Fe^{2+}, Fe^{3+} and Ti.

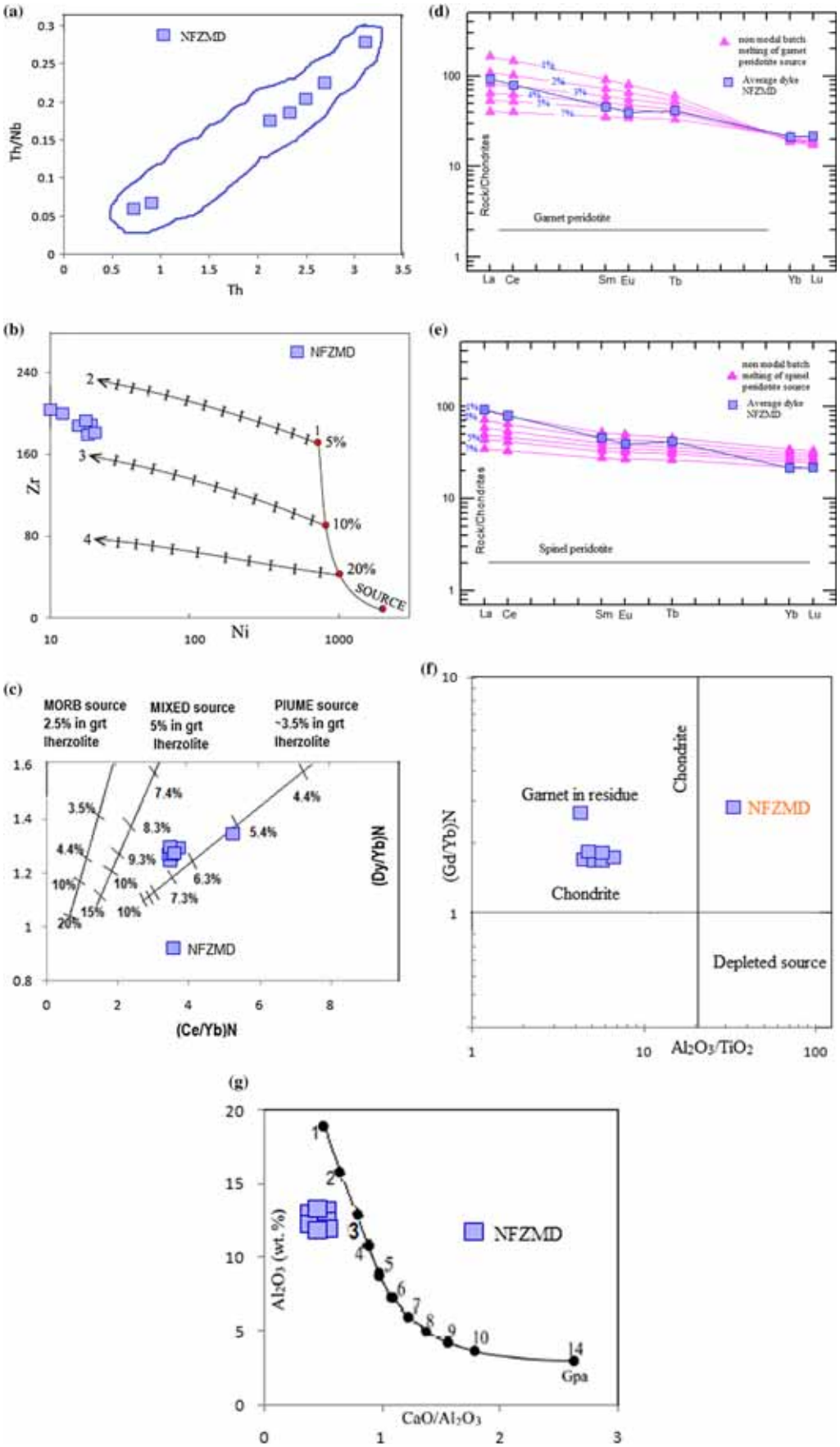
(a)
NFZMD
Th/Nb
Th
(b)
NFZMD
Zr
Ni
5%
10%
20%
SOURCE
(c)
MORB source
2.5% in grt
lherzolite
MIXED source
5% in grt
lherzolite
PIUME source
~3.5% in grt
lherzolite
(Dy/Yb)N
(Ce/Yb)N
NFZMD
(d)
non modal batch
melting of garnet
peridotite source
Average dyke
NFZMD
Rock/Chondrites
Garnet peridotite
La Ce Sm Eu Tb Yb Lu
(e)
non modal batch
melting of spinel
peridotite source
Average dyke
NFZMD
Rock/Chondrites
Spinel peridotite
La Ce Sm Eu Tb Yb Lu
(f)
Garnet in residue
Chondrite
Chondrite
NFZMD
Depleted source
(Gd/Yb)N
Al2O3/TiO2
(g)
NFZMD
Al2O3 (wt.%)
CaO/Al2O3
Gpa

enrichment and moderate to high fractionation of HREE and thus suggests that the parental magmas are derived by partial melting of a mantle source at variable depths (Jourdan *et al.* 2007; Buslov *et al.* 2010). The higher values of Dy/Yb ratios (1.94–2.07) of the samples than chondrites (Dy/Yb = 1.49) point towards derivation from garnet bearing lherzolite source which is reflected in the (Dy/Yb) *vs.* $(Ce/Yb)_N$ plot (Hasse and Devey 1996). The cluster of NFZMD samples on the plume tie line suggests their derivation by 5.4–7.3% melting of lherzolite mantle source with 3.5% garnet (figure 9c). Finally, the non-modal batch melting models considering garnet peridotite and spinel peridotite source indicates assignment of garnet peridotite source for the studied NFZMD. As compared to spinel peridotite source the melting of garnet peridotite source affects the HREE patterns with increasing degrees of melting (figure 9d and e). The observed LREE pattern of the studied dykes (NFZMD) can be derived by 3–5% partial melting of garnet peridotite source (figure 9d). The batch melting equations of Shaw (1970) are adopted for batch melting model and other related details are given in the caption of figure 9.

The Al_2O_3/TiO_2 *vs.* $(Gd/Yb)_N$ plot (after Arndt 2003) indicates garnet stability field corresponding to an enriched mantle source (figure 9f). Herzberg (1995) used CaO/Al_2O_3 ratio of mafic rocks to monitor the depth of magma generation with time. The NFZMD samples cluster at 12.64% Al_2O_3 and 0.52 for CaO/Al_2O_3 ratio, which is consistent with segregation of primary magmas at 2.5–3.5 GPa interval suggesting a melting depth of ∼65–80 km (figure 9g). The studied samples cluster tightly to the left of the experimentally determined mantle solidus indicating reduction of CaO/Al_2O_3. Fractionation of clinopyroxene or a source region having low CaO/Al_2O_3 may cause reduction of CaO/Al_2O_3 (Herzberg 1995).

6.1.2 *Fractional crystallization*

Fractional crystallization is a major process in the evolution of many igneous rocks and is frequently the cause of trends seen on variation diagrams for igneous rocks (Rollinson 1993). The overall major oxide compositions suggest that fractional crystallization has played an important role in the evolution of the present mafic dykes. The magmatic fractionation process is controlled dominantly by the crystallization of plagioclase and clinopyroxene. MgO content (4.68–5.32) and Mg# (44–47) as compared to primitive mantle (Mg# 63–73; Green 1971) reflects an evolved nature of the samples. Higher content of Si, Fe, Ti and K coupled with Mg# (<60) points to nonpicritic flows (Winter 2010). The lower values of Ni (10–19 ppm) and Cr (34–85 ppm) from the NFZMD as compared to primary mantle melt (where Ni = 235–400 ppm, Cr > 400 ppm; Sato 1977) indicates an olivine dominated source implying widespread fractional crystallization and pronounced magmatic evolution and derivation from an iron rich mantle (Winter 2010).

In the variation diagram of SiO_2 *vs.* major oxides, P_2O_5, alkalies and TiO_2 increase while MgO

Figure 9. **(a)** Th *vs.* Th/Nb plot (Allegre and Minster 1978) showing single trend for partial melting represented by good linear correlation for NFZMD. **(b)** Petrogenetic model after Rajamani *et al.* (1985) based on Zr and Ni. (1) Batch melting curve of assumed lherzolite mantle source (11 ppm Zr and 2000 ppm Ni) at 1500°C (1 atm equivalent) with degrees of melting noted in percents. (2, 3, and 4): Olivine fractionation curves with percentage of olivine removal represented in 5% increments. The NFZMD samples appear to be formed by ∼5– <10% batch melting of a lherzolite source followed by > 50% fractional crystallization of olivine. **(c)** $(Dy/Yb)_N$ *vs.* $(Ce/Yb)_N$ diagram for NFZMD clustering along the plume tie lines. Magma sources and degrees of melting noted in percentage are referred to Hasse and Devey (1996). (**d** and **e)** Chondrite-normalized calculated REE patterns in the melting range of 1–7% (F = 0.01–0.07) equilibrium non-modal batch melting of garnet peridotite and spinel peridotite sources. Twice the REE contents than the chondrite (Taylor and McLennan 1995) are assumed for these mantle sources. The distribution coefficients are considered from Hanson (1980) and McKenzie and O' Nions (1991). Mantle source mineralogy of garnet peridotite (Ol:Opx:Cpx:gt = 0.70:0.20:0.07:0.03) after Basu *et al.* (1993); spinel peridotite (Ol:Opx:Cpx:spl = 0.53:0.24:0.20:0.03) after Vijaya Kumar *et al.* (2015). The mineral proportion of garnet peridotite (Ol:Opx:Cpx:gt = 0.2:0.2:0.3:0.3) after Ellam (1992); and spinel peridotite (Ol:Opx:Cpx:spl = 0.01:0.3:0.61:0.08). As compared to spinel peridotite source the melting of garnet peridotite source affects the HREE patterns with increasing degrees of melting (figure 9d and e). The plotted observed average REE pattern of NFZMD indicate best match towards 3–5% melting of garnet peridotite source (figure 9d). **(f)** The Al_2O_3/TiO_2 *vs.* $(Gd/Yb)_N$ plot (after Arndt 2003) indicating garnet stability field corresponding to an enriched mantle source. **(g)** Al_2O_3 *vs.* CaO/Al_2O_3 (weight percent) diagram of Herzberg (1995) showing the pressure in GPa (numbers 1–14 represent the pressure in GPa) along the experimentally determined mantle solidus. The NFZMD samples plot between the 2.5 and 3.5 GPa interval suggesting a melting depths of ∼60–80 km.

and Al_2O_3 decrease with differentiation of SiO_2 suggesting plagioclase and pyroxene fractionation during the evolution of magma (figure S3). Mg number exhibits a negative correlation with TiO_2, P_2O_5 and FeOt and a positive covariation with CaO and Al_2O_3 suggesting low pressure differentiation for the magma involving plagioclase and pyroxene (figure S4). To visualise the crystallization trends, some major oxides and trace elements were plotted against Zr, where all the plots show good crystallization trend (figures S5–S6). The Zr *vs.* trace element plots present positive correlation with (Ba, Y, Ce) Zr, but Cr and Ni shows strong negative correlation. These variation diagrams point towards the genetic relationship of the samples and derivation from common parental magma by simple differentiation process. The decrease in MgO, FeOt and CaO with increase in SiO_2 is consistent with the removal of early formed plagioclase, olivine and pyroxene from cooling liquid. A distinct olivine fractionation trend in the parent magma is observed in MgO *vs.* Fe_2O_3t plot (figure S8). Absence of any significant Eu anomaly indicates minimum role of feldspar during crystallization. In the Rayleigh fractional crystallization model of melt compositions presented in figure 10 for progressive removal of crystals at 20% intervals, labelled as $F = 1$, 0.8, 0.6, 0.4, the chondrite normalized pattern moves to higher relative concentrations with progressive fractional crystallization.

6.1.3 *Crustal contamination*

La/Nb ratio is considered as a suitable index of crustal contamination in magmas (Thompson *et al.* 1983). The dykes show La/Nb ratios >1 (1.81–1.94) confining to a restricted range with respect to CFB (0.5–7). This reflects limited crustal contamination of parent magma (Peate *et al.* 1999; Song *et al.* 2001). Low Th concentrations (0.7–3.1 ppm) also support minimum crustal contamination (Lai *et al.* 2012). The $(Th/Nb)_{PM}$ *vs.* $(La/Nb)_{PM}$ plot (as shown by Zhu *et al.* 2008) for testing crustal contamination of the NFZMD points to lower crustal contamination of the dyke producing magma (figure 11). The higher values of HFSE such as Zr/Nb (15.04–16.42) and Th/Nb (0.06–0.28) ratios reflects lower Nb concentrations which point towards contamination of tholeiitic melts by endogenous contamination caused due to recycling of lithosphere (having depleted upper mantle materials) during subduction of oceanic slab into the mantle (Polat *et al.* 1999). The concentration of Rb (23–89) indicates limited crustal

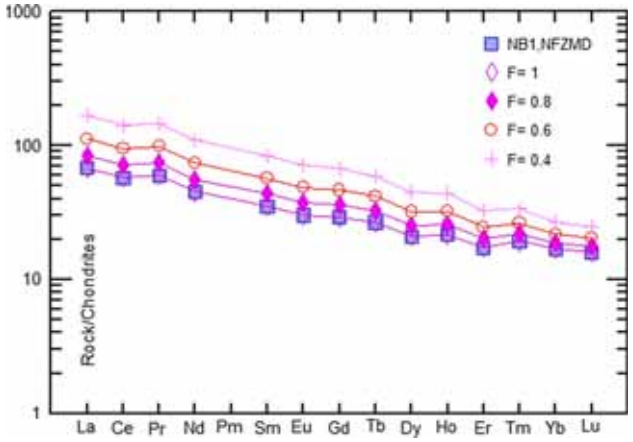

Figure 10. Rayleigh fractional crystallization model for chondrite normalized REE pattern in progressive removal of crystals at 20% interval labelled as $F = 1$, 0.8, 0.6, and 0.4. REE compositions of the sample NB1 of NFZMD is considered as parental composition. Modal mineralogy (Ol:Opx:Cpx:gt = 0.70:0.20:0.07:0.03) is adopted from Basu *et al.* (1993). Mineral partition coefficients for fractional crystallization model are after Rollinson (1993). The chondrite normalized values are after Nakamura (1974).

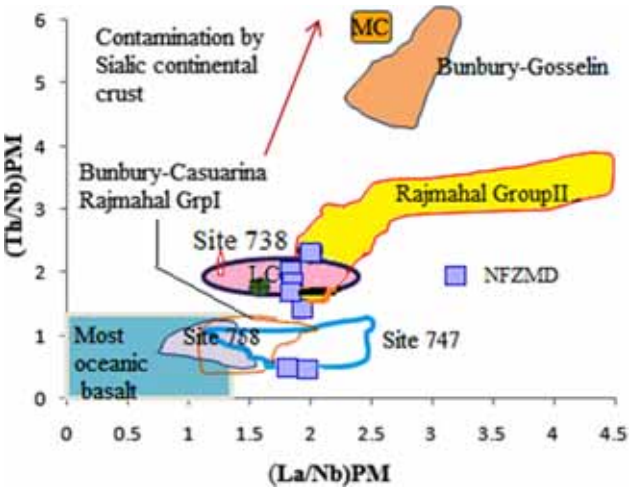

Figure 11. $(Th/Nb)_{PM}$ *vs.* $(La/Nb)_{PM}$ plot for testing crustal contamination of the NFZMD as shown by Zhu *et al.* (2008). Data: 747, 738, 758 and most oceanic basalt from Frey *et al.* (1996, 2002); middle crust (MC), lower crust (LC) from Rudnick and Gao (2003); Bunbury–Gosselin basalt from Frey *et al.* (1996); and Rajmahal Group II basalts from Kent *et al.* (1997). It is noted that NFZMD might have contaminated by lower continental crust.

contamination. Relatively high TiO_2/P_2O_5 (6.14–7.14) can be compared to an intrapalate OIB source, least affected by contamination from granitic continental crust. Primitive mantle-normalized multi-element patterns of NFZMD (figure 5c) marked by positive Ba anomalies and distinct Rb troughs imply minimum input from granitic continental crust.

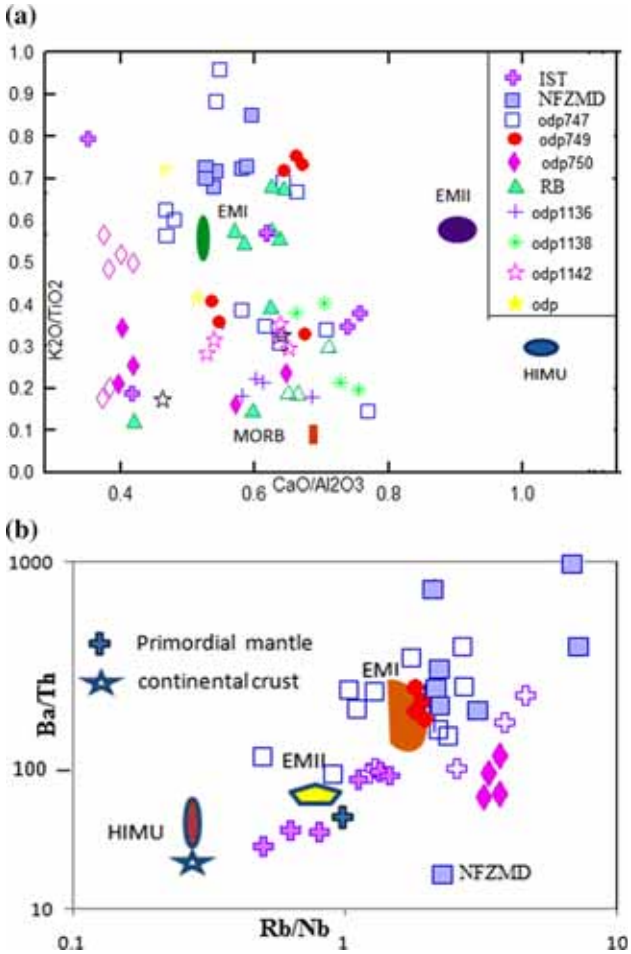

Figure 12. (**a**) Binary plots of K_2O/TiO_2 *vs.* CaO/Al_2O_3 plots in EM1 field. (**b**) Ba/Th *vs.* Rb/Nb plot for NFZMD compared to HIMU, EMI and EMII reservoir (after Weaver 1991). Plots of Rajmahal trap (RB), Sylhat trap (IST, STGB) and Kerguelen ODP sites are shown for comparison. *Data sources*: Frey *et al.* (1996, 2002); Neal *et al.* (2002); Storey *et al.* (1992); and Kent *et al.* (1997). Data for Sylhat trap tholeiites are after Ghatak and Basu (2011) and Islam *et al.* (2014).

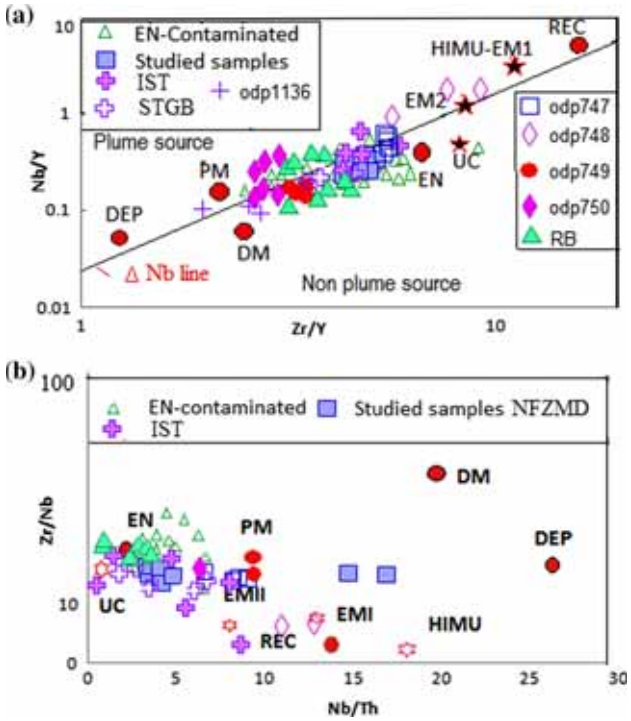

Figure 13. (**a**) Zr/Y *vs.* Nb/Y and (**b**) Nb/Th *vs.* Zr/Nb plot for NFZMD. Plots of Rajmahal trap (RB), Sylhat trap (IST, STGB) and Kerguelen ODP sites are presented for comparison. *Data sources*: Frey *et al.* (1996, 2002); Neal *et al.* (2002); Storey *et al.* (1992); and Kent *et al.* (1997). Data for Sylhat trap tholeiites are after Ghatak and Basu (2011) and Islam *et al.* (2014). NFZMD samples show similar distribution to the En components of Kerguelen basalts as shown by Condie (2005).

6.2 *Nature and source of dyke producing magma*

The major oxide ratios of NFZMD such as CaO/Al_2O_3 (0.40–0.60), $MgO/(MgO + FeO)$ (0.32–0.35), $CaO/(CaO + MgO)$ (0.50–0.60) and $(Na_2O + K_2O)/SiO_2$ (0.07–0.12), indicates CFB like enriched mantle source (Manson 1967; Condie 1981; table S1). The binary plots of K_2O/TiO_2 *vs.* CaO/Al_2O_3 (Jackson and Dasgupta 2008) indicates EM1 field (figure 12a). The Primitive mantle normalized multielement pattern and chondrite normalized REE represent relatively higher abundance of LILE and LREE, which suggest that the parent magma had a mantle source with enrichment of these elements. Zr/Nb ratio ranging from 15.04–16.82 indicates strongly enriched character. Higher values of Nb (11.2–13.2 ppm) and Zr (182–204) contents with respect to NMORB (Nb = 2.33 ppm, Zr = 74 ppm) and lower than that of OIB (Nb = 48 ppm, Zr = 280 ppm) point towards their generation from enriched mantle source (Sun and McDonough 1989). Zr/Sm (26–28) ratios against respective primitive mantle values of 25 attest to an enriched mantle source for the derivation of parent magma producing NFZMD. Trace element ratios like Zr/Nb, La/Nb, Ba/Nb/, Ba/Th, Rb/Nb, Th/Nb, Th/La and Ba/La maintain distinctive values corresponding to different mantle sources and provide constraints on the mantle source components (Weaver 1991). The similar incompatible trace element ratios of NFZMD (table S2) to those of EMI component (Weaver 1991) imply for a parent magma having an enriched mantle (EMI) source. The Ba/Th (46–247), Ba/La (3.96–28.51) and Th/Nb (0.08–0.13) ratios of NFZMD being compatible with an EMI source suggest enrichment of source by oceanic crust and lithospheric components recycled through ancient subduction processes

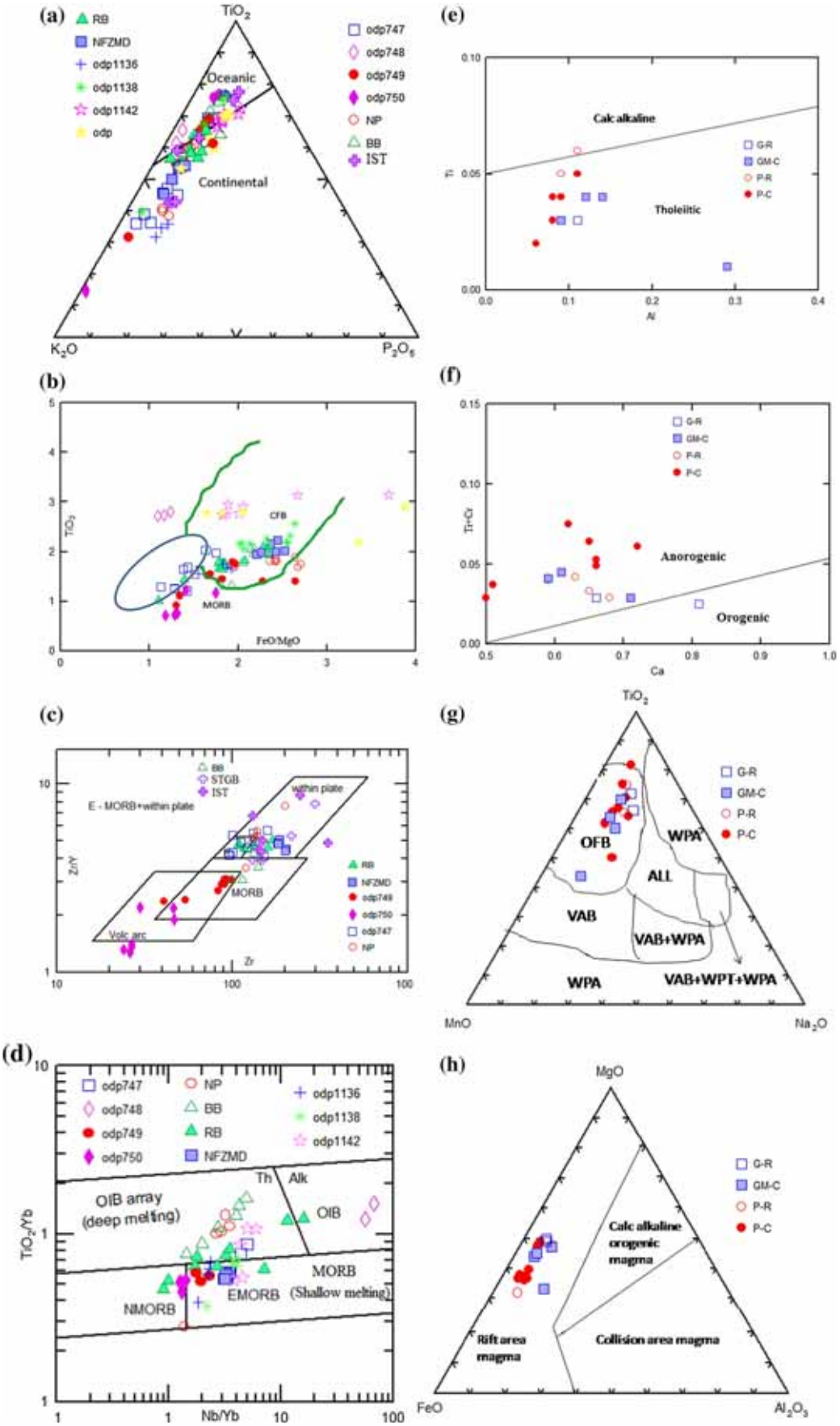
(a)
RB
NFZMD
odp1136
odp1138
odp1142
odp
odp747
odp748
odp749
odp750
NP
BB
IST
Oceanic
Continental
TiO2
K2O
P2O5
(b)
CFB
MORB
TiO2
FeO/MgO
(c)
BB
STGB
IST
E - MORB+within plate
within plate
MORB
Volc arc
RB
NFZMD
odp749
odp750
odp747
NP
Zr/Y
Zr
(d)
odp747
odp748
odp749
odp750
NP
BB
RB
NFZMD
odp1136
odp1138
odp1142
Th
Alk
OIB array
(deep melting)
OIB
MORB
(Shallow melting)
EMORB
NMORB
TiO2/Yb
Nb/Yb
(e)
Calc alkaline
Tholeiitic
G-R
GM-C
P-R
P-C
Ti
Al
(f)
G-R
GM-C
P-R
P-C
Anorogenic
Orogenic
Ti+Cr
Ca
(g)
TiO2
G-R
GM-C
P-R
P-C
OFB
WPA
ALL
VAB
VAB+WPA
WPA
VAB+WPT+WPA
MnO
Na2O
(h)
MgO
G-R
GM-C
P-R
P-C
Calc alkaline orogenic magma
Rift area magma
Collision area magma
FeO
Al2O3

(Weaver 1991; Song *et al.* 2001). The logarithmic Rb/Nb *vs.* Ba/Th plot NFZMD samples also support EM1 source of the dyke (figure 12b). Thus parent magma for NFZMD is characterized by an OIB-like mantle enriched by ancient subducted and recycled oceanic crust giving rise to a source with an EMI signature.

6.3 *Mantle plume signatures*

HFSE ratios such as Zr/Nb, Zr/Y, Nb/Y provide viable petrogenetic clues to trace the plume signature in the genesis of basalts. In terms of Nb/Th, Nb/Y and Zr/Y, NFZMD are similar to oceanic plateau basalts suggestive of mantle plume source (figure 13a and b). It has been suggested that plume derived basalts have lower Zr/Nb ratios in comparison with N-MORB (Zr/Nb: >301). Relatively lower values of Zr/Nb ratios (15.04–16.42) of NFZMD suggest a plume origin for parent magma. Generally (La/Sm) <1 in N-MORB, whereas, plume related MORB have (La/Sm) >1. The present samples show La/Sm > 1. The plume nature of rocks was identified by Fitton *et al.* (1997) and Baksi (2000) using Nb, Y, and Zr. Fitton *et al.* (1997) suggested that if ΔNb (= log(Nb/Y) + 1.74 − 1.92 × log(Zr/Y)) value of any sample is more than 0, it may be derived from a plume source. Baksi (2000) has presented this in a diagram in which log(Zr/Y) has been plotted against log(Nb/Y). Specimens lying above the ΔNb line are inferred to be of plume derived (Baksi 2000) nature. All samples from the present study is close to zero (ΔNb < 0) and plot beyond the ΔNb line (figure 13a). Almost all OIB generally plot above the ΔNb line in the plume field defined by Fitton *et al.* (1997). But a group of Kerguelen basalt has a significant contribution from the enriched component EN, probably continental lithosphere. EN component contributed significantly to the early flood basalts (Bunbury, Rajmahal) and ODP (738) with significant contribution from EN below the ΔNb line (Condie 2005). Contamination of plume sourced OIB like magma with continental crust can produce hybrid magmas with ΔNb < 0. However, the contaminated basalts can be readily distinguished from N-MORB through its higher concentration of most highly incompatible elements. Thus, the negative value of ΔNb for the present samples is attributed to contamination by continental crust. In Nb/Th *vs.* Zr/Nb plot NFZMD samples cluster in EN field specified for enriched component (figure 13b). Condie (2005) used the Zr/Nb–Zr/Y–Nb/Th relations as geochemical fingerprints to distinguish plume head and tail sources for Kerguelen basalts, which are presented here for comparison. Based on Nd–Pb isotopic characteristics, Wilson (1993) opined that Early Cretaceous super plumes all have a strong EMI signature. Thus, EM1 signature of the studied dykes indicate plume source for the dyke rocks. In the (Dy/Yb) *vs.* $(Ce/Yb)_N$ plot (Hasse and Devey 1996) also clusters of NFZMD samples on the plume tie line points towards plume derived source (figure 9c).

6.4 *Tectonic setting of dyke emplacement*

The major oxide ratios such as CaO/Al_2O_3, MgO/(MgO + FeO), CaO/(MgO + CaO), $Na_2O + K_2O$ and $(Na_2O + K_2O)/SiO_2$ shows similar character with CFB (table S1; Manson 1967; Condie 1981). In the TiO_2–K_2O–P_2O_5 plot the samples cluster in the continental field (figure 14a). The samples cluster in CFB field in FeO/MgO *vs.* TiO_2 plot (Fodor and Vetter 1984; figure 14b). Similar behaviour is observed in FeOt–MgO–Al_2O_3 plot and Zr/Y–2Nb–Y plot (figures not shown). The Zr *vs.* Zr/Y tectonic discrimination diagram (after Pearce and Norry 1979) represents within plate

Figure 14. **(a)** K_2O–TiO_2–P_2O_5 plot showing continental tectonic setting. **(b)** FeO/MgO *vs.* TiO_2 plot (Fodor and Vetter 1984) showing CFB nature. **(c)** The Zr *vs.* Zr/Y tectonic discrimination diagram (after Pearce and Norry 1979) showing within plate (WPB) tectonic setting of the samples. **(d)** Nb/Yb *vs.* TiO_2/Yb plot the studied samples indicating E-MORB field. (**e** and **f**) Plots of Rajmahal trap (RB), Sylhat trap (IST, STGB) and Kerguelen ODP sites are presented for comparison. *Data sources*: Frey *et al.* (1996, 2002); Neal *et al.* (2002); Storey *et al.* (1992); and Kent *et al.* (1997). Data for Sylhat trap tholeiites are after Ghatak and Basu (2011) and Islam *et al.* (2014). Tectonic discrimination diagrams (after Leterrier *et al.* 1982) based on the composition of clinopyroxene (calculated on the basis of 6 atoms of oxygen), for mafic dyke rocks from study area. **(e)** Ti *vs.* Al (total) plot show tholeiitic affinity for NFZMD. **(f)** Ti + Cr *vs.* Ca indicating extensional/anorogenic tectonic setting. **(g)** TiO_2–Na_2O–MnO Triangular diagram (after Nisbet and Pearce 1977) indicating OFB field. VAB: volcanic arc basalt; OFB: ocean floor basalt; WPT: within plate tholeiite; and WPA: within plate alkali basalt. **(h)** MgO–FeO–Al_2O_3 diagram (after Le Bas 1962) indicating rift related magmatism.

(WPB) tectonic setting of the samples (figure 14c). The dykes have Al_2O_3/TiO_2 ratio ranging from 5.56–6.61 with respect to Island Arc Basalt (15–25) and MORB (10–15) support the generation of these rocks in an intraplate setting (Regelous *et al.* 2003; Safonova 2009). In the Nb/Yb *vs.* TiO_2/Yb plot the studied samples cluster in the EMORB field (figure 14d). Similar EMORB affinity is also observed in Ce_N–Sr_N–Sm_N discrimination diagram (figure not shown).

The Cpx compositions also delineate similar tectonic setting of the parent magma type. The liquid with tholeiitic affinity crystallize Ca-rich Cpx of the augite–Fe–augite series. The low acmite, Ti and Al content of Cpx also infers to be crystallized in a subalkaline (tholeiitic basalts) environment. The Ti *vs.* Al diagram (after Leterrier *et al.* 1982; figure 14e) has shown the tholeiitic nature of the rock. The Ti + Cr *vs.* Ca plot indicate extensional/anorogenic affinity for the dykes (figure 14f). In the triangular plot of TiO_2–Na_2O–MnO (after Nisbet and Pearce 1977; figure 14g) the samples are mostly concentrated in the field of OFB (ocean floor basalt) while a few show a WPB tendency suggesting an extensional setting for the parent magma. Moreover, the MgO–FeO–Al_2O_3 triangular diagram (after Hout *et al.* 2002; figure 14h) indicates rift related magmas.

6.5 *Geothermobarometry based on mineral composition*

Mineral chemistry can effectively provide an important means of tracking P–T conditions during crystallization (Merceier 1980; Gasparik 1984; Berman 1988). Out of various geothermometers and geobarometers recommended by different workers, some methods based on pyroxene composition, pyroxene-liquid composition and iron oxide pairs have been adopted in the present study using available microprobe data.

6.5.1 *Pyroxene geothermobarometry*

Pyroxene contain the most complete record of the crystallization history of basaltic magma for the long period during which pyroxene crystallize from first stage of crystallization in cores of large phenocrysts (together with olivine) to the late stage of microcryst crystallization in matrix. In the present study, compositions of pyroxene are used for estimation of both temperature and pressure.

6.5.1.1 *Cpx geothermometer*: Different Cpx thermometers advocated by different authors (Lindsley 1983; Putrika *et al.* 1996, 2003; Soesso 1997; Nimis and Taylor 2000; Putrika 2008) are adopted in order to deduce the equilibration temperatures of Cpx of the studied dykes. The procedure of Lindsley's (1983) graphical thermometer, the very accurate method of determining pyroxene temperature involves simple recalculation of some important molecules (like Ac, Jd, FecaTs, CrcaTs, AlcaTs, etc.) and plotting those with experimentally determined pyroxene thermometer contours. When projected to this diagram, the pyroxene compositions of the dykes clearly show a temperature range from 1250°–800°C (figure 15). In the figure, the majority of the Cpx data fall in between 1200° and 1000°C isotherms. Only two data plots fall in around 800°C, because of anomalies in Na_2O and TiO_2 contents. The temperature estimates of Cpx liquidus ($\sim$1000–1190°C) depict that the Cpx is crystallized later than or together with Plag.

Soesso (1997) advocated an empirical approach to derive eigen vector grids for P and T using principal component analysis of the major element composition of Cpx crystallized from melting experiments. He suggested that eigenvectors (X_{PT}, Y_{PT}) calculated from correlation matrix of large experimental dataset of igneous Cpx stabilized in a wide P–T range (P-1-34 kbar, T = 1000–1470°C) can be used to deduce the P–T stability of Cpx in host magmas. The derived X_{PT} and Y_{PT} values of Cpx from the dyke rocks predict a temperature range of 1050–1150°C and pressure less than 2 kbar for Cpx crystallization in the dyke magma (figure 16a and b).

Cpx chemistry is also used to estimate temperature and pressure using a geothermobarometers calibrated by Putrika *et al.* (1996, 2003) and Putrika (2008). The temperature ranges from 1003–1030°C using the equations T_1 and P_1 from Putrika *et al.* (1996). The equation T_1 uses the jadeite–diopside/hedenbergite exchange equilibrium and work as a geothermometer. Equation P_1 is particularly sensitive to jadeite formation and uses the temperature calculated in T_1 to calculate pressure in kbar. The estimated average temperature from Putrika *et al.* (2003) is 1050°C. When the equations 32d (T) and 32c (P) are used from Putrika (2008), the average temperature of crystallization of Cpx is calculated as 903°C and 1045°C. The equations 33 (T) and 34 (T) of Putrika (2008) based on Cpx composition only are also employed as geothermometer and calculated

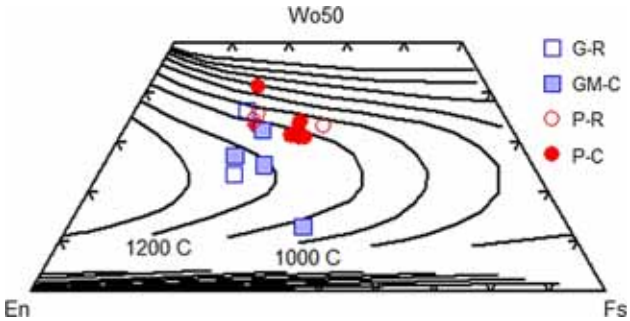

Figure 15. Graphical pyroxene thermometry (after Lindsley 1983). PC, PR, GC and GR denote phenocryst core, phenocryst rim, groundmass core and groundmass rim.

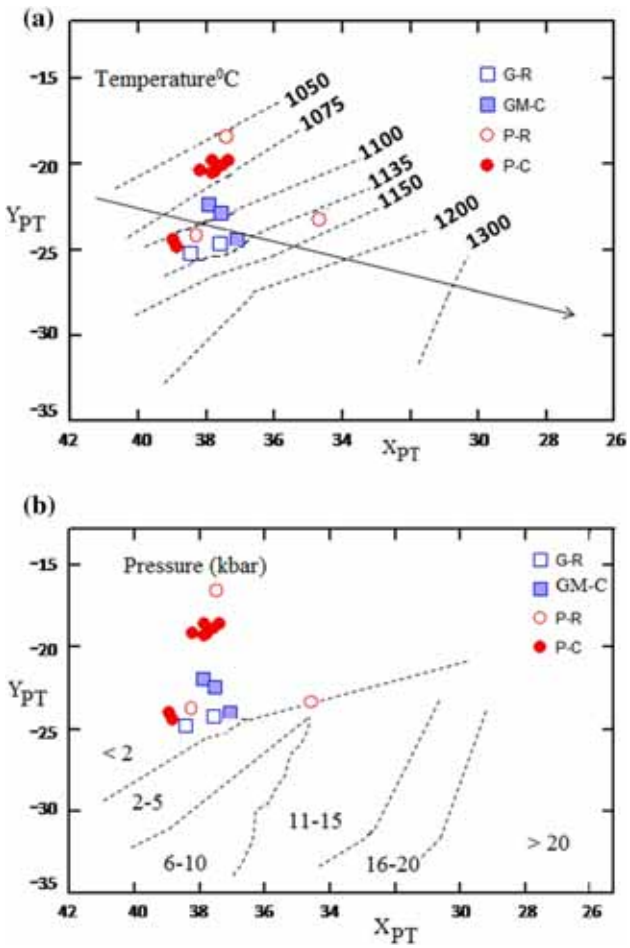

Figure 16. (**a**) X_{PT}–Y_{PT} thermometric plot of Cpx from mafic dyke of NFZMD. Isotherms (broken lines) are shown after (Soesso 1997). Arrow denotes the direction of low pressure Cpx modifications due to oxide mineral saturation. (**b**) X_{PT}–Y_{PT} barometric plot of Cpx from NFZMD. Pressure fields are shown after Soesso (1997).

average T is 975.4°C and 1116.3°C. Geothermometer of Nimis and Taylor (2000) estimate temperatures ranging from 995° to 997.3°C. Thus the average crystallization temperature of the dyke

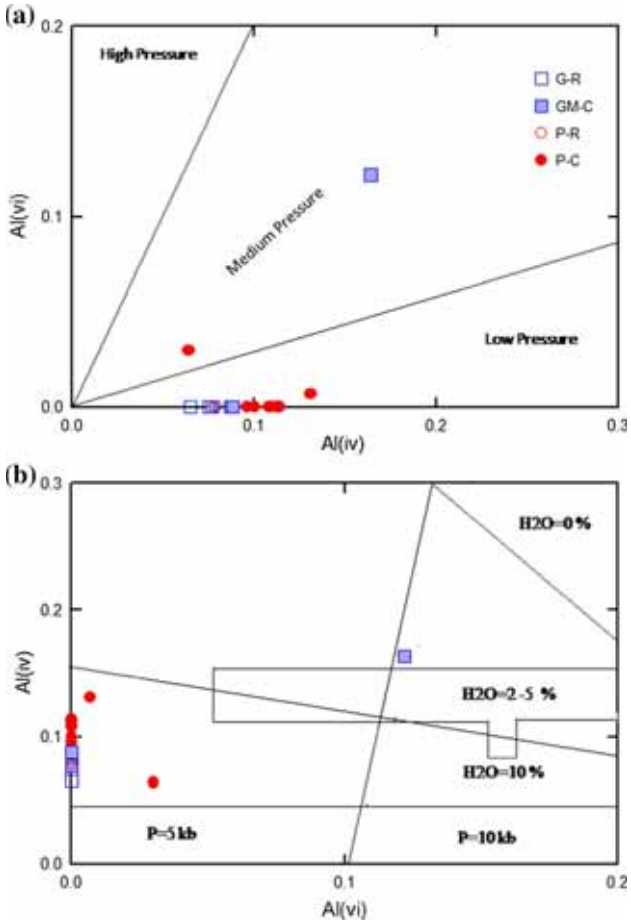

Figure 17. (**a**) Al^{vi}/Al^{iv} diagram (Aoki and Shiba 1973) for pressure estimation of the clinopyroxenes of volcanic rocks. (**b**) Al^{iv}/Al^{vi} plot (Heltz 1973) for pressure estimation of the clinopyroxenes in volcanic rocks.

rocks calculated from different methods put forwarded by different authors ranges from 800° to 1250°C (table 5).

6.5.1.2 *Cpx geobarometer*: The pressures are estimated on the basis of multivariate analysis of clinopyroxene (Soesso 1997), Cpx-liquid equilibria (Putrika 1996, 2008; Putrika *et al.* 2003), geobarometer of Nimis (1995) and Nimis and Taylor (2000) based on crystal structure modelling to estimate the pressure of crystallization of the dyke rocks. The plot of Al^{iv}/Al^{vi} (after Aoki and Shiba 1973) and Al^{vi}/Al^{iv} plot (Helz 1973) of Cpx are also used to estimate the pressure. The geobarometer of Putrika (2008) gave a pressure range of 1.2–1.8 kbar while that of Soesso indicates pressures < 2 kbar (figure 16b). In the Al^{iv}/Al^{vi} plot of Cpx (after Aoki and Shiba 1973) the dyke rocks indicate low pressure (figure 17a). The Al^{vi}/Al^{iv} plot (Helz 1973) shows that the Cpx has crystallized <5 kb pressure and the water content of the parental

magma was ∼10% (figure 17b). The other methods give mostly negative values and therefore results are not presented. These barometers might not be calibrated for low pressures. Thus, the estimated pressure calculated from different methods suggests < 2 kb pressure of crystallization of the dyke rocks. A summary of the deduced T and P obtained by different methods and their significance is given in table 6.

6.5.2 *Two oxide geothermometry: Magnetite–ilmenite geothermometer*

The methods of geothermometry put forwarded by Powell and Powell (1977), Lindsley and Spencer (1982) and Anderson and Lindsley (1985) for estimation of equilibration temperatures are adopted in the present study. ILMAT, a magnetite–ilmenite geothermometry Program (version 1.20) formulated by Lepage (2003) is used based on the recalculation schemes of Carmichael (1967), Anderson (1968), Lindsley and Spencer (1982) and Stormer (1983). The calculated value of ulvospinel and ilmenite molecule percentages ranges from 52.17–53.11% and 95.32–95.82%, respectively. The equilibration temperatures of Fe–Ti oxides are between 817° and 798°C, as per the thermometer of Powell and Powell (1977), 695° to 727°C as per the thermometer of Lindsley and Spencer (1982) while it ranges from 749° to 721°C as per Anderson and Lindsley (1985). Thus, the temperature range estimated from different methods vary from 695 to 817°C, which reflects that the Cpx crystallization is earlier than Fe–Ti oxide minerals re-equilibration and thus the Cpx temperatures represent the approximate eruption temperature of the dyke rocks. The Fe–Ti oxide phases appear to be late crystallizing phases. The summary of equilibration temperature of Fe–Ti oxide estimated from different methods is presented in table 6.

6.6 *Evaluation of oxygen fugacity*

Oxygen fugacity of the studied dykes is evaluated from both Cpx composition and Fe–Ti oxides to estimate the crystallization history as it plays a vital role in changing the liquidus temperature, melt and crystals composition, the controlling magmatic processes, the crystallization sequences and types of crystallized minerals (Moretti 2005; France *et al.* 2010). To obtain oxygen fugacity, the $Al^{iv} + Na$ *vs.* $Al^{vi} + 2Ti + Cr$ diagram (after Schweitzer *et al.* 1979) based on the amount of 3 valent iron present in Cpx is used. It is accepted that the Fe^{3+} in pyroxenes depends on the amount of Al^{vi} which means it depends on aluminium balance in tetrahedral and octahedral positions. This diagram is framed on the aluminium balance in the tetrahedral position with Cr^{+} in the octahedral position. The figure shows that the Cpx in the studied dykes had probably crystallized under low oxygen fugacity and are hence plotted below the Fe^{3+} line indicating low oxygen fugacity (figure 18). The oxygen fugacity (–log fO_2) values are derived by using the mathematical solution (Spencer and Lindsley 1981; table 6). The values of –log fO_2 and equilibration temperatures of Fe–Ti oxides of the present study are plotted in figure 19. The majority of the data is close to the QFM curve (after Eugster and Wones 1962), the Quartz–Fayalite–Magnetite synthetic buffer (figure 19). It is suggested that during crystallization of the studied mafic dykes, prevailing −log fO_2 followed the values of a fayalite–magnetite–quartz buffer curve, indicating the tholeiitic composition of varied nature.

6.7 *Regional significance of the data: Implications for genetic link to Kerguelen plume*

It is suggested that the Kerguelen plume played a significant role for supply of heat to the lithosphere that fragmented eastern Gondwana land (Coffin *et al.* 2002; Ingle *et al.* 2002a, b). The Ninetyeast Ridge (NER), Broken Ridge, Bunbury basalts, Naturaliste plateau, and Kerguelen plateau in the southern Indian Ocean (figure 1, Weis and Frey

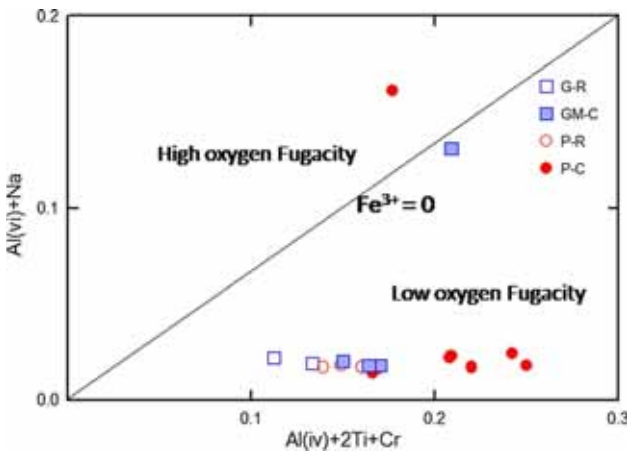

Figure 18. Al(vi) + Na *vs.* Al(iv) + 2Ti + Cr diagram for oxygen fugacity estimation (Schweitzer *et al.* 1979).

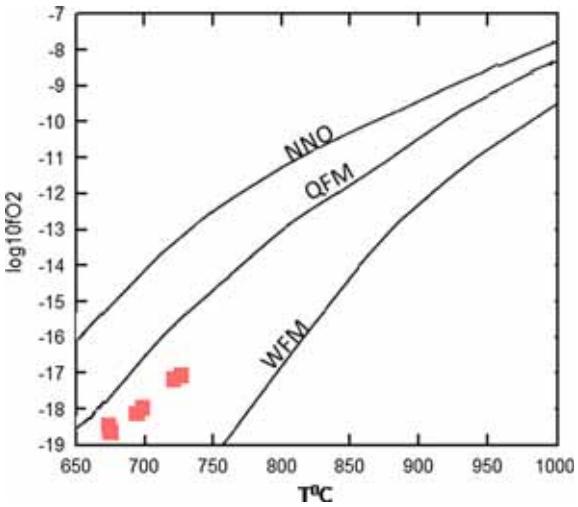

Figure 19. Temperature of equilibration *vs.* oxygen fugacity of Fe–Ti oxides. NNO, QFM and WM represent buffer curves for Nickel–Nickel, Quartz–Fayalite–Magnetite and Wutzite–Magnetite buffers, respectively (after Eugster and Wones 1962).

1991; Frey *et al.* 1996, 2000) have strong relation to this plume. Based on geochronological, geochemical data and plate reconstructions, some of the earlier workers opined that the Rajmahal–Sylhet–Bengal Traps (116 ± 3.5 Ma) defining continental flood basalt province in eastern India is related to the early episode of Kerguelen volcanism (figure 1) (Baksi 1995; Ghatak and Basu 2011; Islam *et al.* 2014). Storey *et al.* (1992) differentiated the Rajmahal basalts into Groups I and II on the basis of Ti/Zr and Zr/Y ratios for a given value of MgO and the presence of an Indian Ocean E-MORB component was also marked in the plume.

The Sylhet Traps as well as the Late Cretaceous ultramafic–mafic alkaline carbonatitic magmatic activity (Sarkar *et al.* 1996; Nambiar and Golani 1998; Srivastava and Sinha 2004) documents the Mesozoic magmatism in the Shillong plateau. Ghatak and Basu (2011) have correlated the Rajmahal basalts with the Sylhet Traps (Shillong plateau) ∼550 km to the east by their geochemical similarities and Nd, Sr and Pb isotopic signatures and opined for extended Rajmahal flood basalt province through Bengal basin to the Shillong plateau. Similar correlation is suggested by Islam *et al.* (2014) for some Sylhet Trap basalts and advocated for Kerguelen mantle plume head in Bengal basin.

The major oxide plots of the studied dykes of the Shillong plateau show similarity with Kerguelen plume derived tholeiites (figure 4a and b). The LREE enriched chondrite normalized REE pattern is similar to the Group II Rajmahal basalt (Kent *et al.* 2002), Sylhet trap basalt (MB) that is believed to be Kerguelen plume derived basalt (figure 5a). This LREE enrichment is also similar to ODP sites 747, 1136, 1138, 1141 and 1142 Kerguelen lavas (figure 5b). In the multielement diagram also similar pattern is observed with Rajmahal basalts, Sylhet basalts (MB, Ghatak and Basu 2011) as well as Kerguelen plateau ODP sites (figure 5c and d). Moreover, similar contamination by lower continental crust compared to Kerguelen plume derived basalts is marked for NFZMD (figure 11). The presence of an EMI component in some older Kerguelen plateau lavas (sites 747) has been discussed by Frey *et al.* 2002). The similar EM1 signatures of the present samples are observed in the plots (figure 12a and b). When compared with the distribution of basalts from Kerguelen plateau as shown by Condie (2005), NFZMD point towards EN field specified for enriched component (figure 13a and b). Besides, similar tectonic setting of NFZMD with some of the Kerguelen plume derived tholeiites is noticed in figure 14(a–d). The binary plots of $(Th/Nb)_{PM}$ *vs.* $(Nb/Zr)_{PM}$, Zr/Y *vs.* Ti/Zr and MgO *vs.* Ti/Zr for NFZMD indicates similar attributes to Kerguelen plume derived basalts (figure 20a–c). The affinity of the present dyke samples for Group II Rajmahal basalts (Kent *et al.* 2002) is well depicted in figure 20(b and c). The chondrite normalized REE pattern suggests garnet peridotite mantle source of NFZMD. Similar garnet peridotite source is corroborated to the basalt flows of Mawsynram–Shella basalts of Sylhat volcanic in East Khasi Hills section (Ghatak and Basu 2011).

The Plag ($An_{51.4}$–$An_{71.4}$) and Cpx (average $Wo_{34}En_{42}Fs_{23}$) mineral chemistry are found to be similar to Kerguelen plume derived Rajmahal tholeiites (An_{73}–An_{53} between core and rim of Plag). Groundmass plag is less calcic in both ($An_{58–60}$ in Rajmahal tholeiite and $An_{51.5–59.6}$ in NFZMD). Similarly, Cpx of Rajmahal tholeiites range in composition from augite to ferroaugite with minor compositional difference between phenocrysts $En_{48–46}Wo_{39–35}Fs_{19–14}$. Pigeonite is common in groundmass in both and is intermediate between magnesian and ferriferous pigeonite (Ghosh and Kent 2003). The eruption temperatures deduced for NFZMD are in good agreement with eruption temperatures reported for the Rajmahal tholeiites (about 1120°C) estimated from two pyroxene geothermometer equilibration (Sarkar *et al.* 1989). Similar compositions of Cpx are also presented by Sylhat trap tholeiites (figure 6a).

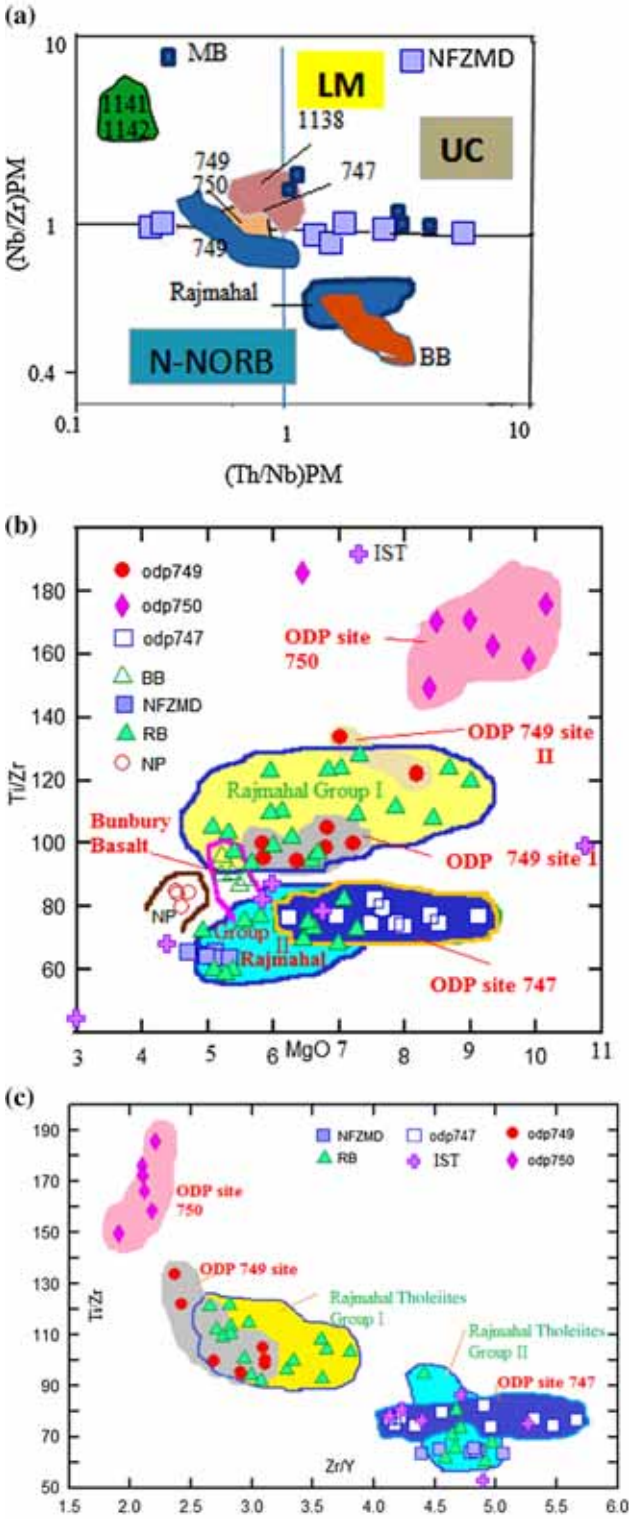

Figure 20. **(a)** $(Th/Nb)_{PM}$ *vs.* $(Nb/Zr)_{PM}$ plot showing similarities with Kerguelen plume derived basalts and Sylhet Trap basalts (MB, Ghatak and Basu 2011); **(b)** Plot of MgO *vs.* Ti/Zr for NFZMD and Rajmahal volcanics indicating Rajmahal Group II field. **(c)** Zr/Y *vs.* Ti/Zr plot for NFZMD clustering in the field of Rajmahal tholeiites of Group II. *Data sources*: Frey *et al.* (1996, 2002); Neal *et al.* (2002); and Storey *et al.* (1992). Data for Sylhat trap (IST) are after Islam *et al.* (2014).

The Nongchram fault of the Shillong plateau is presumably of Cretaceous age formed by the Kerguelen plume related domal uparching (Gupta and Sen 1988; Golani 1991). The studied mafic dykes being directionally parallel to this N–S trending fault may indicate genetic link to the Kerguelen mantle plume.

7. Summary and concluding remarks

- The integrated petrochemical and phase petrographic signatures point to a common parent tholeiitic magma source and decipher subalkaline nature of the NFZMD. The major, trace and REE geochemistry of the studied rocks suggest that the present rocks are the products of extensive differentiation of mantle derived alkaline basaltic magma. The enrichment in LREE relative to HREE and HFSE, systematic Nb anomalies, moderate MREE to HREE fractionation suggests variable depths of melting of slightly enriched mantle source in the garnet stability field. As per geochemical modelling, the studied dykes are derived by 3–5% non-modal batch melting of garnet peridotite source at melting depth of ∼65–80 km. The parent magma for NFZMD indicates an OIB-like mantle enriched by ancient subducted and recycled oceanic crust giving rise to a source with an EMI signature indicating mantle plume source. Trace element behaviour indicates some amount of crustal contamination of the parent magma by lower continental crust. Finally, the petrochemistry as well as Plag and Cpx mineral chemistry of NFZMD suggest that these subalkaline mafic dykes have probably been generated by tholeiitic magmas in an anorogenic extensional environment and indicate *in-situ* intracontinental emplacement of the dykes through fault controlled fissures, which is supported by the tectonic setting of the area (Nambiar 2007; Gupta and Sen 1988). The deep seated Nongchram fault generated during an important tectonomagmatic event in Shillong plateau in Early to Late Cretaceous time might serve as conduits for mantle material of NFZMD.
- Cpx temperatures (1250–800°C) represent the approximate emplacement temperature of NFZMD. Independent barometers indicate that Cpx in the dykes crystallized over a range of pressures of less than 2 kbar (1.2–1.8 kbar). Based on Aluminium balance, it can be inferred

that Cpx in the studied dykes have crystallized under low oxygen fugacity. Fe–Ti oxide temperatures and $-\log fO_2$ data follow the trend of QFM curve pointing towards more evolved tholeiitic composition indicating that NFZMD rocks suffered more fractionation at medium to low temperatures under decreasing oxygen fugacity during cooling of NFZMD.

- The very good correlation of REE behaviour and other trace element behaviour of the studied dykes with Kerguelen plume derived Rajmahal Group II basalt, Sylhet volcanics and some ODP sites from Kerguelen basalts implicate to a genetic link of the dykes with the Kerguelen mantle plume. But we need more geochemical data, especially good isotopic data to get a clear picture of NFZMD.

Acknowledgements

The author is thankful to the Department of Science and Technology, Govt. of India for extending financial support for the work (SR/FTP/ES-40/2011). The anonymous reviewers are gratefully acknowledged for their thorough and incisive review of this paper. Their constructive comments and suggestions have significantly improved the manuscript. I am indebted to Prof Santosh Kumar, Kumaun University, Nainital for his kind support and encouragement. Finally, the work is dedicated to late Prof Kali Prasad Sarma, Gauhati University, Assam, my PhD mentor, who inspired and encouraged me for pursuing research.

References

Acharyya S K, Mitra N D, Nandy D R 1986 Regional geology and tectonic setting of north east India and adjoining region; *Geol. Surv. India* **119** 6–12.

Allegre C J and Minster J F 1978 Quantitative models of trace element behaviour in magmatic process; *Earth Planet. Sci. Lett.* **38** 1–25.

Anderson A T 1968 Oxidation of the La Blanche Lake titaniferous magnetite deposit, *Québec J. Geol.* **76(4)** 528–547.

Anderson D J and Lindsley D H 1985 New (and final!) models for the Ti-magnetite/ilmenite geothermometer and oxygen barometer. Abstract AGU 1985 Spring Meeting Eos Transactions; *Am. Geophys. Union* **66(18)** 416.

Aoki K I and Shiba I 1973 Pyroxenes from Lherzolite Inclusions of Itinome–Gata, Japan; *Lithos* **6** 41–51.

Arndt N 2003 Komatiites, kimberlites, and boninites; *J. Geophys. Res.* **108** 1–11.

Baksi A K 1995 Petrogenesis and timing of volcanism in the Rajmahal flood basalt province, Northeastern India; *Chem. Geol.* **121** 73–90.

Baksi A K 2000 Search for a deep-mantle component in mafic lavas using Nb–Y–Zr plot; *Canadian J. Earth Sci.* **38** 813–824.

Basu A R, Renne P R, Das Gupta D K, Teichman F and Poreda R J 1993 Early and late alkali igneous pulses and a high 3 He plume origin for the Deccan flood basalts; *Science* **261** 902–906.

Berman R 1988 Internally consistent Thermodynamic data for minerals in the system Na_2O–K_2O–MgO–FeO–Fe_2O_3–Al_2O_3–SiO_2–TiO_2–H_2O–CO_2; *J. Petrol.* **29** 445–522.

Bilham R and England P 2001 Plateau 'pop-up' in the great 1897 Assam Earthquake; *Nature* **410** 806–809.

Bondre N R, Hart W K and Sheth H C 2006 Geology and geochemistry of the Sangamner mafic dike swarm, Western Deccan Volcanic Province, India: Implications for regional stratigraphy; *J. Geol.* **114** 155–170.

Buslov M M, Safonova I Yu, Fedoseev G S, Reichow M, Davies C and Babin G A 2010 Permo-Triassic plume magmatism of the Kuznetsk Basin, Central Asia: Geology, geochronology and geochemistry; *Russian Geol. Geophys.* **51** 901–916.

Carmichael I S E 1967 The iron–titanium oxides of salic volcanic rocks and their associated ferromagnesian silicates; *Contrib. Mineral. Petrol.* **14(1)** 36–64.

Chakrabarty R, Basu A R, Bandopadhyay P K and Zou H 2011 Age and origin of Chilka anorthosites, Eastern Ghats, India: Implications for massif anorthosites petrogenesis and breake up of Rodinia; In: *Topics in Igneous Petrology* (eds) Ray J S *et al.*, Springer Science, 355–382.

Chottopadhyay N and Hashimi S 1984 The Sung Valley alkaline-ultramafic carbonatite complex, East Khasi Hills and Jaintia Hills district, Meghalaya; *Rec. Geol. Surv. India* **113(4)** 23–24.

Coffin M F, Pringle M S, Duncan R A, Gladezenko T P, Storey M, Müller R D and Gahagan L A 2002 Kerguelen hotspot magma output since 130 Ma; *J. Petrol.* **43** 1121–1139.

Condie K C 1981 Archaean Greenstone belts, Elsevier, Amsterdam, 434 p.

Condie K C 2005 High field strength element ratios in Archean basalts: A window to evolving sources of mantle plumes? *Lithos* **79** 491–504, https://doi.org/10.1016/j.lithos.2004.09.014.

Condie C K, Bobrow D J and Card K D 1987 Geochemistry of Precambrian Mafic Dykes from the Southern Superior Province of the Canadian Shield; In: *Mafic dyke swarms* (eds) Halls H C and Fahring W F, *Geol. Assoc. Can. Spec. Paper* **34** 95–108.

Dasgupta S and Nandy D R 1982 Seismicity and tectonics of Meghalaya plateau, Northeast India; *Proc. VII symp. On Earthquake Engineering, Roorkee* **1** 19–24.

Delaney P T, Pollard D D, Ziony J I and McKee E H 1986 Field relations between dikes and joints: Emplacement processes and paleostress analysis; *J. Geophys. Res.* **91** 4920–4938.

Devi N R and Sarma K P 2006 Tectonostratigraphic study of conglomerates of Shillong basin of Meghalaya, India; *J. Geol. Soc. India* **68** 1100–1108.

Devi N R and Sarma K P 2010 Strain analysis and stratigraphic status of Nongkhya, Sumer and Mawmaram

conglomerates of Shillong basin, Meghalaya, India; *J. Earth Syst. Sci.* **119(2)** 161–174.

Devi N R 2018 An overview of geochemical significance of cretaceous mafic dykes in and around Nongchram Fault Zone of Shillong Plateau, NE India: Implications for genetic link to Kerguelen plume; *Int. J. Curr. Trends Sci. Tech.* **8(03)** 20,181–20,199.

Duraiswami R A and Shaikh T N 2013 Geology and geochemistry of the saucer-shaped sill near Mahad, western Deccan Traps, India and its significance to the Flood Basalt Model 556. *Bull. Volcanol.* **75** 1–18.

Dostal J and Durning M 1998 Geochemical constrains on origin and evolution of early mesozoic dikes in Atlantic Canada; *Eur. J. Mineral.* **10** 79–93.

Ellam R 1992 Lithospheric thickness as a control on basalt geochemistry; *Geology* **20** 153–156.

Ermenco N A, Negi B S, Nasianov M V, Seregin A M, Despande B G, Sengupta S N, Talukdar S N, Sastri V V, Sokaluv I P, Pavbukov A T, Dutta A K and Raju A T R 1969 Tectonic map of India–Principles of preparation; *Bull. ONGC* **6(1)** 1–111.

Ernst R E, Buchan K L and Palmar H C 1995 Giant dyke swarms, characteristics, distribution and geotectonic applications; In: *Physics and Chemistry of Dykes* (eds) Baer G and Haemann A, A. A. Balkema, Rotterdam, pp. 3–21.

Eugster H P and Wones D R 1962 Stability relations of the ferruginous biotite, annite; *J. Petrol.* **3** 82–125.

Evans P 1964 The tectonic framework of Assam; *J. Geol. Soc. India* **5** 88–96.

Fitton J G, Saunders A D, Norry M J, Hardarson B S and Taylor R N 1997 Thermal and chemical structure of the Iceland plume; *Earth Planet. Sci. Lett.* **153** 197–208.

Fodor R V and Vetter S K 1984 Riftzone magmatism: Petrology of basaltic rocks transitional from CFB to ORB, southeastern Brazil margin; *Contrib. Mineral. Petrol.* **88** 307–321.

France L, Koepke J, Ildefonse B, Cichy S B and Deschamps F 2010 Hydrous partial melting in the sheeted dike complex at fast spreading ridges: experimental and natural observations; *Contrib. Mineral. Petrol.* **160** 683–704.

French J E, Haeman L M, Chacko T and Srivastava R K 2008 1891–1883 Ma Southern Bastar–Cuddapah mafic igneous events, India: A newly recognized large igneous province; *Precamb. Res.* **160** 308–322.

Frey F A, Mc Naughton N J, Nelson D R, deLaeter J R and Duncan R A 1996 Petrogenesis of the Bunbury basalt, Western Australia: Interaction between the Kerguelen plume and Gondwana lithosphere? *Earth Planet. Sci. Lett.* **144** 163–183.

Frey F A, Coffin M F, Wallace P J, Weis D and Zhao X 2000 Origin and evolution of a submarine large igneous province: The Kerguelen Plateau and Broken Ridge, southern Indian Ocean; *Earth Planet. Sci. Lett.* **176** 73–89.

Frey F A, Weis D, Borisova A Y and Xu G 2002 Involvement of continental crust in the formation of the Cretaceous Kerguelen Plateau: New perspectives from ODP leg 120 sites; *J. Petrol.* **43** 1207–1239.

Gasparik T 1984 Two Pyroxene Thermobaometry with new Experimental data in the system in CaO–MgO–Al_2O_3–SiO_2; *Contrib. Mineral. Petrol.* **87** 87–97.

Ghatak A and Basu A R 2011 Vestiges of the Kerguelen plume in the Sylhet Traps, Northeastern India; *Earth Planet. Sci. Lett.* **308** 52–64.

Ghosh N C and Kent R W 2003 The Rajmahal Basalts: A review of their geology, composition and Petrogenesis; *Memoir Geol. Soc. India* **53** 167–196.

Golani P R 1991 Nongchram fault: A major dislocation zone from western Meghalaya; *J. Geol. Soc. India* **12** 56–62.

Gupta R P and Sen A K 1988 Imprints of Ninety-East Ridge in the Shillong Plateau, Indian Shield; *Tectonophys.* **154** 335–341.

Hanson G N 1980 Rare Earth Elements in Petrogenetic studies of igneous systems; *Ann. Rev. Earth Palnet. Sci.* **8** 371–406.

Harijan N, Sen A K, Sarkar S, Das J D and Kanungo D P 2003 Geomorphotectonics around the Sung valley carbonatite complex, Shillong plateau, NE India: Remote sensing and GIS approach; *J. Geol. Soc. India* **62(1)** 103–109.

Hasse K M and Devey C W 1996 Geochemistry of lavas from the Ahu and Tupa volcanic fields, Easter Hotspot, South Pacific: Implications for intrapalate magma genesis near a spreading axis; *Earth Planet. Sci. Lett.* **157(1–4)** 129–143.

Heltz R T 1973 Phase relations of basalts in their melting ranges at $PH_2O = 5$ kb as a function of oxygen fugacity, Part1. Mafic phases; *J. Petrol.* **14(2)** 249–302.

Hergberg C 1995 Generation of plume magmas through time: An experimental approach; *Chem. Geol.* **126** 1–16.

Hout F, Hebert R, Varfalvy V, Beaudoin G, Wang C S, Liu Z F, Cotton J and Dostal J 2002 The Beimarang Melange (Southern Tibet) brings additional constraints in asseing the origin, metamorphic evolution and obduction processes of the Yarlung Zangbo Ophiolite; *J. Asian Earth Sci.* **21** 307–322.

Ingle S, Weis D and Frey F A 2002a Indian continental crust recovered from Elan Bank, Kerguelen Plateau (ODP Leg 183, Site 1137); *J. Petrol.* **43** 1241–1257.

Ingle S, Weis D, Scoates J S and Frey F A 2002b Relationship between the early Kerguelen plume and continental flood basalts of the paleo-Eastern Gondwana margins. *Earth Planet. Sci. Lett.* **197** 35–50.

Irvine T N and Baragar W R A 1971 A guide to the chemical classification of the common volcanic rocks; *Canadian J. Earth Sci.* **8** 523–548.

Islam M S, Meshesha D and Shinjo R 2014 Mantle source characterization of Sylhet Traps, northeastern India: A petrological and geochemical study; *J. Earth Syst. Sci.* **123(8)** 1839–1855.

Jackson M G and Dasgupta R 2008 Compositions of HIMU, EM1, and EM2 from global trends between radiogenic isotopes and major elements in ocean island basalts; *Earth Planet. Sci. Lett.*, https://doi.org/10.1016/j.epsl.2008.09.023.

Jensen L S 1976 A new cation plot for classifying subalkalic volcanic rocks; *Misc. Pap.* **66**, Ont. Depart. of Mines, Ottawa, Canada.

Johnson S Y and Alam A M N 1991 Sedimentation and tectonics of the Sylhet trough Bangladesh; *Geol. Soc. Am. Bull.* **103** 1513–1527.

Jourdan F, Bertrand H, Scharer U, Blichert-Toft J, Feraud G and Kampunzu A B 2007 Major and trace elements and Sr, Nd, Hf, and Pb isotope compositions of the Karoo Large Igneous Province, Botswana, Zimbabwe: Lithosphere *vs.* mantle plume contribution; *J. Petrol.* **48** 1043–1077.

Kayal J R 2001 Microearthquake activity in some parts of the Himalaya and the tectonic model; *Tectonophys.* **339** 331–351.

Kent R W, Saunders A D, Kempton P D and Ghose N C (eds) 1997 Rajmahal basalts, eastern India: Mantle sources and melt distribution at a volcanic rifted margin; *Geophys. Monograph (AGU),* Washington DC, pp. 145–182.

Kent R W, Pringle M S, Muller R D, Saunders A W and Ghose N C 2002 $^{40}Ar/^{39}Ar$ geochronology of the Rajmahal basalts, India, and their relationship to the Kerguelen Plateau; *J. Petrol.* **43** 1141–1153.

Khanna P P, Saini N K, Mukherjee P K and Purohit K K 2009 An appraisal of ICP-MS technique for determination of REEs: Long term QC assessment of Silicate rock analysis; *Himalayan Geol.* **30(1)** 95–99.

Kontak D J, Jensen S M, Dostal J, Archibald D A and Kyser T K 2001 Cretaceous Mafic Dyke Swarm, Pearlyland, Northenmost Greenland: Geochronology and Petrology; *Can. Mineral.* **39** 997–1020.

Lai S, Qin J, Li Y, Li S and Santosh M 2012 Permian high Ti/Y basalts from the eastern part of the Emeishan Large Igneous Province, southwestern China: Petrogenesis and tectonic implications; *J. Asian Earth Sci.* **47** 216–230.

Le Bas M J 1962 The role of aluminium in igneous clinopyroxene with relation to their parentage; *Am. J. Sci.* **260** 267–288.

Le Bas M J, Le Maitre R W, Streckeisen A and Zanemn B 1986 A chemical classification of volcanic rocks based on the total alkali–silica diagram; *J. Petrol.* **27** 745–750.

Lepage L D 2003 ILMAT: An excel worksheet for ilmenite–magnetite geothermometry and geobarometry; *Comput. Geosci.* **29(5)** 673–678.

Le Roex A P and Lanyon R 1998 Isotope and trace element geochemistry of Cretaceous Damaraland lamprophyre and carbonatites, northwestern Namibia: Evidence for plume–lithosphere interactions; *J. Petrol.* **39** 1117–1146.

Lindsley D H 1983 Pyroxene thermometry; *Am. Mineral.* **68** 477–493.

Lindsley D H and Spencer K J 1982 Fe–Ti oxide geothermometry: Reducing analyses of coexisting Ti–magnetite (Mt) and ilmenite (Ilm) abstract AGU 1982 Spring Meeting Eos Transactions; *Am. Geophys. Union.* **63(18)** 471.

Leterrier J, Maury R C, Thoron P, Girard D and Marchal M 1982 Clinopyroxene composition as a method of identification of the magmatic affinities of paleovolcanic series; *Earth Planet. Sci. Lett.* **59** 139–154.

Manson V 1967 Geochemistry of basaltic rocks in Poldervaart treatise on rocks of basaltic composition; Intersci. Publ. John Wiley & Sons, New York, pp. 215–269.

McKenzie D amd O'Nions R 1991 Partial melt distributions from inversion of rare earth element concentrations; *J. Petrol.* **32** 1021–1091.

Merceier J C C 1980 Single Pyroxene Thermometry; *Tectonophys.* **70** 1–37.

Mitra S K 1998 Structural history of the rocks of the Shillong Group around Sohiong, east Khasi hills, Meghalaya; *Indian J. Geol.* **70** 123–131.

Miyashiro A 1974 Volcanic rock series in island arcs and active continental margins; *Am. J. Sci.* **274** 321–355.

Moretti R 2005 Polymerisation, basicity, oxidation state and their role in ionic modelling of silicate melts; *Ann. Geophys.* **56** 340–368.

Mitchell R H, Platt R G, Downey M and Laderoute D G 1991 Petrology of alkaline lamprophyres from the Coldwell alkaline complex, northwestern Ontario; *Can. J. Earth Sci.* **28** 1653–1663.

Morimmoto N 1988 The Nomenclature of Pyroxenes; *Mineral. Mag.* **52** 425–433.

Murthy N G K 1987 Mafic dyke swarms of the Indian Shield; In: *Mafic Dyke Swarms* (eds) Halls H C and Fahring W F, *Geol. Assoc. Canada Spl. Paper* **34** 393–400.

Nakamura N 1974 Determination of REE, Ba, Fe, Mg, Na, and K in carbonaceous and ordinary chondrites; *Geochim. Cosmochim. Acta.* **38** 757–775.

Nambiar A R 1987 Alkaline magmatism in parts of East Garo Hills and West Khasi Hills districts, Meghalaya; *Rec. Geol. Surv. India* **115** 25–41.

Nambiar A R 2007 Petrology of lamprophyres from parts of East Garo Hills and West Khasi Hills districts, Meghalaya; *J. Geol. Soc. India* **32** 125–136.

Nambiar A R and Golani P R 1985 A new find of carbonatite from Meghalaya; *Curr. Sci.* **54** 281–282.

Nandy D R 2001 Geodynamics of northeastern India and the adjoining region; *Acad. Publ. Kolkata*, pp. 111–130.

Neal C R, Mahoney J J and Chazey W J 2002 Mantle sources and the highly variable role of continental lithosphere in basalt petrogenesis of the Kerguelen Plateau and Broken Ridge LIP: Results from Ocean Drilling Program Leg 183; *J. Petrol.* **43** 1177–1206.

Nimis P 1995 A clinopyroxene geobarometer for basaltic systems based on crystal-structure modelling; *Contrib. Mineral. Petrol.* **121** 115–125.

Nimis P and Taylor W R 2000 Single Clinopyroxene Thermobarometry for Garnet peridotite. Part 1. Calibaration and Testing of the Cr-in Cpax Barometer and an Enstatite in Cpx Thermometer; *Contrib. Mineral. Petrol.* **139** 541–554.

Nisbet E G and Pearce J A 1977 Clinopyroxene composition in mafic lavas from different tectonic settings; *Contrib. Mineral. Petrol.* **63** 149–160.

Pearce J A and Norry M J 1979 Petrogenetic implications of Ti, Zr, Y and Nb variations in volcanic rocks; *Contrib. Mineral. Petrol.* **69** 33–47.

Peate D W, Hawkesworth C J, Mantovani M S M, Rogers N W and Turner S P 1999 Petrogenesis and stratigraphy of the high Ti/Y Urubici magma type in the Paraná flood basalt province and implications for the nature of 'Dupal'-type mantle in the South Atlantic region; *J. Petrol.* **40** 451–473.

Polat A, Kerrich R and Wyman D A 1999 Geochemical diversity in oceanic komatiites and basalts from the late Archean Wawa greenstone belts, Superior Province, Canada: Trace element and Nd isotope evidence for a heterogeneous mantle; *Precamb. Res.* **94** 139–173.

Powell R and Powell M 1977 Geothermometry and oxygen barometry using coexisting iron-titanium oxides: A reappraisal; *Mineral. Mag.* **41(318)** 257–263.

Putirka K, Johnson M, Kinzler R, Longhi J and Walker D 1996 Thermobarometry of mafic igneous rocks based on clinopyroxene-liquid equilibria, 0–30 kbar; *Contrib. Mineral. Petrol.* **123** 92–108.

Putrika K D, Mikaelian H, Ryerson F and Shaw H F 2003 New clinopyroxene-liquid thermobarometers for mafic, evolved and volatile bearing lava compositions, with applications to lavas from Tibet and the Snake River Plain, Idaho; *Am. Mineral.* **88** 1542–1554.

Putrika K D 2008 Thermometers and Barometers for volcanic systems; *Rev. Mineral. Geochem.* **69** 61–120.

Rajamani V, Shivkumar K, Hanson G N and Shirey S B 1985 Geochemistry and petrogenesis of amphibolites, Kolar schist Belt, South India: Evidence for komatitic magma derived by low percentage of melting of the mantle; *J. Petrol.* **96** 92–123.

Rajsekhar R P and Mishra D C 2008 Crustal structure of Bengal Basin and Shillong Plateau: Extension of Eastern Ghat and Satpura mobile belts to Himalayan fronts and seismotectonics; *Gondwana Res.*, https://doi.org/10.1016/j.gr.2007.10.009.

Rao J M 2002 Petrology and geochemistry of dolerite dykes, West Garo Hills, Meghalaya: A preliminary study; *Gondwana Res.* **5(4)** 884–888.

Rao J M, Rao G V S P and Sarma K P 2009 Precambrian mafic magmatism of Shillong Plateau, Meghalaya and their evolutionary history; *J. Geol. Soc. India* **73** 143–152.

Ray J, Saha A, Koeberl C, Thoni M, Ganguly S and Hazara S 2013 Geochemistry and Petrogenesis of Proterozoic mafic rocks from East Khasi Hills, Shillong Plateau, Northeastern India; *Precamb. Res.* **230** 119–137.

Regelous M, Hofmann A W, Abouchami W and Galer S J G 2003 Geochemistry of lavas from the Emperor seamounts, and the geochemical evolution of Hawaiian magmatism from 85 to 42 Ma; *J. Petrol.* **44** 113–140.

Robertson E A M, Biggs J, Cashman K V, Flyod M A and Brown C V 2016 Influence of regional tectonics and pre-existing structures on the formation of elliptical calderas in the Kenyan Rift; In: *Magmatic Rifting and Active Volcanism* (eds) Wright T J, Ayele A, Ferguson D J, Kidane T and Vye-Brown C, *Geol. Soc. London, Spl. Publ.* **420** 43–67.

Rollinson H R 1993 Using Geochemical Data: Evaluation, Presentation, Interpretation, John Wiley, Chichester, 352p.

Rudnick R L and Gao S 2003 The Composition of the Continental Crust, In: *Treatise on Geochemistry* (eds) Holland H D and Turekian K K, Vol. 3, The Crust, Elsevier, Oxford, pp. 1–64.

Safonova I Yu 2009 Intraplate magmatism and oceanic plate stratigraphy of the Paleo-Asian and Paleo-Pacific Oceans from 600 to 140 Ma; *Ore Geol. Rev.* **35** 137–154.

Saini N K, Mukherjee P K, Khanna P P and Purohit K K 2007 A proposed amphibolite reference rock sample (AM-H) from Himachal Pradesh; *J. Geol. Soc. India* **69** 799–802.

Saini N K, Khanna P P, Mukherjee P K and Purohit K K 2013 Preparation and characteristics of two geochemical reference materials: DG-H (granite) and AM-H (amphibolite) from the Himalayan orogenic belt; *Geostand. Geoanal. Res.* **38** 111–122.

Sarkar A, Datta A K, Poddar B C, Bhattacharyya B K, Kollapuri V K and Sanwal R 1996 Geochronological studies of Mesozoic igneous rocks from eastern India; *J. Southeast Asian Earth Sci.* **13** 77–81.

Sarma K P, Venkateshwaralu M, Patil S K, Laskar J J, Devi, N R and Mallikaharjuna R J 2014 Paleomagnetism of metadolerite dykes and sills from Proterozoic Shillong basin, NE India: Implications related to the age and magmatism; *J. Geol. Soc. India.* **83(2)** 147–155.

Sarma K P, Laskar J J, Devi N R, Mazumdar N, Mallikarjuna Rao J and Venkateshwaralu M 2015 Geochemistry of Mesoproterozoic metadolerite dykes and sills of Shillong basin, Meghalaya, NE India; *Asian J. Multidiscip. Studies* **3(2)** 37–47.

Sato H 1977 Nickel content of basaltic magmas: Identification of primary magmas and a measure of the degree of olivine fractionation; *Lithos* **10** 113–120.

Schweitzer E L, Papike J J and Bence A E 1979 Statistical Analysis of Clinopyroxenes from Deep Sea Basalts; *Am. Mineral.* **64** 502–513.

Shaw D M 1970 Trace element fractionation during anatexis; *Geochim. Cosmochim. Acta.* **34** 237–243.

Soesso A 1997 A multivariate statistical analysis clinopyroxene composition: Empirical coordinates for the crystallization PT-estimations; *Geologiska Foreningens I Stockholms Forhandlingar.* **119** 55–60.

Song X Y, Zhou M F, Hou Z Q, Cao Z M, Wang Y L and Li Y 2001 Geochemical constraints on the mantle source of the Upper Permian Emeishan Continental Flood Basalts, Southwestern China; *Int. Geol. Rev.* **43** 213–225.

Spencer K J and Lindsley D H 1981 A solution model for coexisting iron-titanium oxides; *Am. Mineral.* **66(11–12)** 1189–1201.

Srinivasan V 2005 The Dauki Fault in northeast India through remote sensing; *J. Geol. Soc. India* **66** 413–426.

Srivastava R K and Sinha A K 2004 Geochemistry and Petrogenesis of early Cretaceous sub-alkaline mafic dykes from Swangkre–Rongmil, East Garo Hills, Shillong Plateau, NE India; *Proc. Ind. Acad. Sci., Earth Planet Sci.* **113** 683–697.

Srivastava R K, Sivaji Ch and Chalapathi Rao N V 2008 Indian Dykes Through Space and Time: Retrospect and Prospect; In: *Indian dykes: Geochemistry, Geophysics and Geochronology* (eds) Srivastava R K, Ch Sivaji and Chalapathi Rao N V, Narosha Publishing House Pvt. Ltd., New Delhi, India, pp. 1–18.

Storey M, Kent R W, Saunders A D, Hergt J, Salters V J M, Whitechurch H, Sevigny J H, Thirlwall M F, Leat P, Ghose N C and Gifford M 1992 Lower Cretaceous volcanic rocks on continental margins and their relationship to the Kerguelen Plateau; *Proc. Ocean Drilling Prog. Scientific Results* **120** 33–53.

Stormer J C 1983 The effects of recalculation on estimates of temperature and oxygen fugacity from analyses of multi-component iron-titanium oxides; *Am. Mineral.* **68(5–6)** 586–594.

Sun S S and McDonough W F 1989 Chemical and isotopic systematics of oceanic basalts: Implications for mantle composition and processes; *Geol. Soc. London, Spec. Publ.* **42** 313–345.

Taylor S R and McLennan S M 1995 The geochemical evolution of the continental crust; *Rev. Geophysics.* **33** 241–265.

Thompson R N, Morrison M A, Dickin A P and Hendry G L 1983 Continental Flood basalts arachnids rule OK? In: *Continental Basalts and Mantle Xenoliths* (eds) Hawkesworth C J and Norry M J, Shiva Pub. Cambridge, MA, pp. 158–185.

Vijaya Kumar K, Rathna K and Leelanandan C 2015 Proterozoic subduction-related and continental rift zone mafic magmas from the Eastern Ghats Belt; *Curr. Sci.* **108(2)** 184–197.

Weaver B L 1991 The origin of ocean island basalt end member compositions: Trace element and isotopic constraints; *Earth Planet. Sci. Lett.* **104** 381–397.

Weis D and Frey F A 1991 Isotope geochemistry of the Ninety-east Ridge basalts: Sr, Nd, and Pb evidence for the involvement of the Kerguelen hotspot; In: *Proceedings of the Ocean Drilling Program* (eds) Weissel J,

Peirce J, Taylor E and Alt J, **121** College Station TX, pp. 591–610.

Wilson M 1993 Geochemical signatures of oceanic and continental basalts: A key to mantle dynamics? *J. Geol. Soc. London* **150** 977–990.

Winter J D 2010 Principles of Igneous and Metamorphic Petrology; PHI, 693p.

Zhu D, Mo X, Pan G, Zhao Z, Dong G, Shi Y, Liao Z, Wang L and Zhou C 2008 Petrogenesis of earliest early cretaceous mafic rocks from the Cona area of eastern Tethyan Himalaya in south Tibet: Interaction between the incubating Kerguelen plume and the eastern greater India lithosphere? *Lithos* **100** 147–173.

Corresponding editor: Rajneesh Bhutani